Lateral surface pressure generated by nascent ribosomal RNA suppresses growth of fibrillar centers in the nucleolus

Tetsuya Yamamoto[a,b], Tomohiro Yamazaki[c], Kensuke Ninomiya[c], Tetsuro Hirose[c,d]

[a]Institute for Chemical Reaction Design and Discovery, Hokkaido University, Kita 21, Nishi 10, Kita-ku, Sapporo, 001-0021, Japan.
[b]PRESTO, Japan Science and Technology Agency (JST), 4-1-8, Honcho, Kawaguchi, Saitama 332-0012, Japan.
[c]Graduate School of Frontier Biosciences, Osaka University, 1-3 Yamadaoka, Suita 565-0871, Japan.
[d]Institute for Open and Transdisciplinary Research Initiatives, Osaka University, 1-3 Yamadaoka, Suita 565-0871, Japan

The authors declare no conflict of interest.
[1]T. Yamamoto and T. Yamazaki contributed equally.
[2]To whom correspondence should be addressed. E-mail: (Theory) tyamamoto@icredd.hokudai.ac.jp and (Experiment) tyamazaki@fbs.osaka-u.ac.jp

All the authors designed and discussed the research and wrote and revised the paper. T. Yamamoto developed the theoretical model and performed calculations. T. Yamazaki performed the experiments.

ABSTRACT

Liquid-liquid phase separation (LLPS) has been thought to be the biophysical principle governing the assembly of the multiphase structures of nucleoli, the site of ribosomal biogenesis. Condensates assembled through LLPS increase their sizes to minimize the surface energy as far as their components are available. However, multiple microphases, fibrillar centers (FCs), dispersed in a nucleolus are stable and their sizes do not grow unless the transcription of pre-ribosomal RNA (pre-rRNA) is inhibited. To understand the mechanism of the suppression of the FC growth, we here construct a minimal theoretical model by taking into account the nascent pre-rRNAs tethered to the FC surfaces by RNA polymerase I. Our theory predicts that nascent pre-rRNAs generate the lateral osmotic pressure that counteracts the surface tension of the FCs and this suppresses the growth of the FCs over the stable size. The stable FC size decreases with increasing the transcription rate and decreasing the RNA processing rate. This prediction is supported by our experiments showing that RNA polymerase inhibitors increase the FC size in a

dose-dependent manner. This theory may provide insight into the general mechanism of the size control of nuclear bodies.

Nucleolus | Transcription | Phase separation

Significance statement

The nucleolus, a site of pre-ribosomal RNA (pre-rRNA) production, has a characteristic multiphase structure, which has been thought to be assembled through liquid-liquid phase separation (LLPS). Although condensates assembled through LLPS grow by coarsening or coalescence as far as the components are available, the multiple inner phases, fibrillar centers (FCs), are dispersed in a nucleolus. To investigate the underlying mechanism, we constructed a minimal theoretical model by considering nascent pre-rRNAs tethered to RNA polymerase I at the FC surface. This model is supported by our experiments and explains previous experimental observations. This work shed light on the role of nascent RNAs to control the size of nuclear bodies.

INTRODUCTION

In the interchromatin spaces, there are a variety of nuclear bodies, such as nucleoli (1-4), nuclear speckles (5), and paraspeckles (6). Many of the nuclear bodies are scaffolded by ribonucleoprotein (RNP) complexes, which are composed of RNA and RNA-binding proteins (RBPs). The class of RNAs, which are essential to the assembly of specific subcellular bodies, is called architectural RNA (arcRNA) (6-8). A growing number of researches suggest that some nuclear bodies are assembled via liquid-liquid phase separation (LLPS), which is driven by the multivalent interaction between RBPs bound to arcRNAs (6-8). Condensates produced by LLPS are spherical and increase their size by coarsening and/or coalescence due to the surface tension (macroscopic phase separation) (9).

Nucleoli are nuclear bodies, where ribosome assembly takes place (1,2). In the nucleoli, pre-ribosomal RNAs (pre-rRNAs) are transcribed by RNA polymerase I (Pol I) and maturated to construct ribosomes with ribosomal proteins. A nucleolus is not a uniform disordered liquid, but multiple microphases, called fibrillar centers (FCs), are dispersed in the sea of a granular component (GC) (Fig. 1A). Fibrillarins (FBLs), which are RBPs interacting with pre-rRNAs, are condensed to form another phase, called the dense fibrillar component (DFC), at the interfaces between FCs and the GC. The multiphase structures of nucleoli have been thought to be assembled via simple LLPS (10). However,

this picture may not be complete because the FCs do not show coalescence or coarsening to increase their sizes. Indeed, when the Pol I transcription of pre-rRNA is inhibited, FCs show coalescence, as in the case of LLPS, and are excluded to the surface of the nucleolus (the excluded FCs are called nucleolar caps) (11). This implies that transcription somehow suppresses the growth of FCs. Ribosomal DNA (rDNA), from which pre-rRNAs are transcribed, is a repeat sequence of coding units (10 kb) intervened by the intergenic regions (30 kb). The transcriptionally active rDNA units and Pol I are localized at the surfaces of FCs where the transcription of pre-rRNAs takes place (3, 11-13). The DFC layer is probably assembled by the RNP complexes of nascent pre-rRNAs and the associated RBPs, such as FBLs (18). FBLs show phase separation with the physiological concentration and bind to nascent pre-rRNAs (10,13). These experimental results imply that nascent pre-rRNAs may act as `surfactants' that suppress the growth of FCs.

Multiple paraspeckles scaffolded by NEAT1_2 arcRNAs are dispersed in a nucleoplasm (14). This situation is somewhat analogous to FCs in a nucleolus. Paraspeckles form the core-shell structure, where the two terminal regions of NEAT1_2 form the shell and the middle region of NEAT1_2 forms the core (15,16). We have recently shown that the terminal regions of NEAT1_2 in the shell suppresses the growth of paraspeckles, analogous to micelles of triblock copolymers (14,17). The size of paraspeckles increases with the NEAT1_2 transcription upregulation (14,18), which is opposite to the response of FCs in a nucleolus to transcription upregulation. This implies that the size control mechanism of FCs in a nucleolus is different from that of paraspeckles.

We here construct a simple theoretical model that predicts the contributions of nascent pre-rRNAs to the assembly of the multiphase structure of nucleolus. This model takes into account the phase separation, the transcription kinetics, and the interfacial effects, which are probably the minimum to account for the multiphase structure. Our theory predicts that the nascent pre-rRNAs are stretched to accommodate FBLs in the DFC layer and generate the lateral pressure that counteracts with the interfacial tensions. The size of FCs is determined by the balance of the interfacial tensions and the lateral pressure. Our theory predicts that the radius of FCs is proportional to the inverse of the square root of the transcription rate. The suppression of the FC growth by the pre-rRNA transcription results from the fact that these complexes are end-grafted to the FC surfaces via Pol I, in contrast to other condensates in which arcRNAs diffuse freely and increase their sizes by the transcription upregulation. To test our prediction, we experimentally measured the FC sizes and the pre-rRNA levels while the transcription

rate is changed by the dose of BMH-21 or CX-5461, which specifically inhibits the Pol I transcription. The scaling exponent predicted by our theory is consistent with our experimental results, implying that the lateral pressure generated by nascent pre-rRNAs are possible mechanism of the size control of FCs. We anticipate that this theory can be a base theory to further look into the contribution of the multiphase structure in the function of nucleoli and can be extended to study the mechanism of the size control and the functions of other nuclear bodies, such as nuclear speckles and transcriptional condensates.

RESULTS

Model of nucleolus

We here construct a minimal model of a nucleolus to predict the size of FCs in the steady state. The nucleolus is composed of a GC in which multiple spherical FCs are dispersed (Fig. 1A). Pol I molecules (shown by white particles in Fig. 1B) are entrapped in the FCs (shown by a light blue droplet in Fig. 1B). The transcriptionally active repeat units of rDNA (shown by the black line in Fig. 1B) are localized at the surfaces of the FCs. We assume that the number of Pol I molecules N_{pol} and the number of transcriptionally active rDNA units N_{act} in the nucleolus are constant. Nascent pre-rRNAs (shown by chains of green particles in Fig. 1B) are localized at the surfaces of FCs and form a DFC layer (Fig. 1B). Recent experiment revealed that only the 5' terminal external transcribed spacer (ETS) regions of nascent pre-rRNAs are localized at the DFC layer and that, among the proteins localized in the DFC layer, FBLs contributed most significantly to the localization of the terminal regions of nascent pre-rRNAs in the DFC layer (13). Motivated by this result, we take into account only the FBL-binding terminal regions of nascent pre-rRNAs as arcRNAs that scaffolds the DFC layers and only FBLs as RBPs that bind to these regions (see also the Discussion section). Recent experiments also revealed that the upstream half of ETSs are localized at the DFC layer and the downstream half is localized at the FC (13). This motivated us to assume that the terminal regions are spanning from the top to the bottom of the DFC layer. Some RBPs bind to the nascent pre-rRNAs and the others diffuse freely in the DFC layer (shown by magenta particles in Fig. 1B). The interface between FC and DFC is located at a distance r_{in} from the center and the interface between DFC and GC is located at a distance r_{ex} from the center (see Fig. 1B). For simplicity, we assume that all the FCs have equal volume and the sum of the volumes of microphases is fixed to V_{m}. This assumption does not seem so far off although it has not been quantified (19).

The number of nascent pre-rRNAs at the surfaces of FCs is determined by the kinetics of transcription and RNA processing. We treat the transcription dynamics of pre-rRNA by using an extension of the model used by Stasevich and coworkers (20) (Fig. 2). Leaving the kinetic equations to Materials and Methods, we here discuss the processes of transcription and RNA processing that are taken into account in our model, see eqs. 6-10. Pol I in an FC binds to the transcription start site (TSS) of a transcriptionally active rDNA unit. The Pol I bound to the TSS starts transcription (Fig. 2A) or returns to the FC without starting transcription (Fig. 2A). The rate with which the Pol I bound to the TSS starts transcription is smaller than the rate with which this Pol I returns to the FC without starting transcription. The Pol I polymerizes a pre-rRNA while it moves uni-directionally towards the transcription termination site (TTS). The nascent pre-rRNAs are subject to co-transcriptional RNA processing (Fig. 2B). The FBL-binding terminal region is located at the ETS of pre-rRNA and is cleaved co-transcriptionally by endoribonuclease. The average time between the transcription initiation and the cleavage of the FBL-binding region is τ_{pr}, where this time includes the elongation time to the cleavage site and the time necessary for the enzymatic reaction, see Fig. 2B and the Discussion section. Pol I reaches TTS at the average elongation time τ_{e} and is then released to the FC ($\tau_{\mathrm{pr}} < \tau_{\mathrm{e}}$), see Fig. 2C. This model is designed to focus on the transcription of the FBLs of nascent pre-rRNAs and to treat the rest of the process as simple as possible. The kinetic equations of the Pol I transcription and co-transcriptional processing are derived by taking into account the above-mentioned processes, see Fig. 2 and eqs. 6-8. By solving these kinetic equations for the steady state, we found that the surface density σ_{in} is proportional to the radius r_{in} of FCs, see eq. 11 in Materials and Methods. We thus introduce a dimensionless parameter

$$\zeta = N_{\mathrm{r}} \frac{\sigma_{\mathrm{in}} b^3}{r_{\mathrm{in}}}, \qquad [1]$$

which is proportional to the transcription rate and processing time τ_{pr}, while it is independent of the radius r_{in}.

The stability of the system is quantified by the free energy. The free energy F_{d} of a DFC layer has 4 contributions: 1) the elastic free energy f_{ela} of nascent pre-rRNA, 2) the mixing free energy f_{mix} of RBPs and solvent, 3) the interaction free energy f_{int} between RBPs (both freely diffusing in the DFC layer and bound to nascent pre-rRNA), and 4) the binding free energy f_{bnd} of RBPs to the pre-rRNA terminal regions. The expressions of these free energy contributions are shown in eqs. 12–17 in Materials and

Methods. The elastic free energy f_{ela} of flexible polymer chains, such as nascent pre-rRNAs, increases as the chains stretch because the number of possible conformations decreases (9). The thermal fluctuation mixes the components (nascent pre-rRNA units, RBPs, and solvent) and this contribution is quantified as the mixing free energy f_{mix}. The interaction free energy f_{int} is the free energy contribution of the multivalent interactions between RBPs. The binding free energy f_{bnd} represents the free energy gain due to the binding of RBPs to nascent pre-rRNA units and the thermal fluctuations that dissociate RBPs from nascent pre-rRNA units. The free energy F_{d} takes into account the binding of RBPs to the terminal regions of nascent pre-rRNAs and the spherical geometry of the system in an extension of the Alexander model of polymer brush (21).

The free energy F of the system has the form

$$\frac{F}{V_{\mathrm{m}}} = \frac{3}{4\pi r_{\mathrm{in}}^3}\left[F_{\mathrm{d}} + 4\pi r_{\mathrm{in}}^2\gamma_{\mathrm{in}} + 4\pi r_{\mathrm{ex}}^2\gamma_{\mathrm{ex}}\right], \qquad [2]$$

where γ_{in} is the interfacial energy per unit area (interfacial tension) at the interface between FC and DFC ($r = r_{\mathrm{in}}$) and γ_{ex} is the surface energy per unit area (interfacial tension) at the interface between DFC and GC ($r = r_{\mathrm{ex}}$). The external radius r_{ex} is determined by the conservation of the number of RNA units in the DFC layer in the steady state, see eq. 11 in the Materials and Methods. The interfacial tension results from the interactions between the components of interfacing phases. We therefore assume that the surface tensions, γ_{in} and γ_{ex}, are proportional the local volume fraction of RBPs at the interfaces, with the proportional coefficient γ_{p} (see eqs. 18 and 19 in the Materials and Methods). The free energy F_{d} is a functional of the occupancy α_{p} of the pre-rRNA terminal regions by RBPs, the volume fraction ϕ_{p} of RBPs freely diffusing in the DFC layer, and the volume fraction ϕ_{r} of the FBL units, where these are functions of the distance r from the center of the FC.

In our theory, we take into account the non-equilibrium nature of the system via nascent pre-rRNAs produced at the surfaces of FCs by Pol I transcription. One may also think that the continuous addition of RNA units to nascent pre-rRNAs makes the conformations of their terminal regions different from those at the equilibrium. In a simple estimate, the local equilibrium approximation that uses the equilibrium chain conformations is effective in the length scales smaller than the diffusion length $\lambda_{\mathrm{d}}\ (= \sqrt{D_{\mathrm{r}}\tau_{\mathrm{s}}})$, where D_{r} is the diffusion constant of a pre-rRNA unit and τ_{s} is the elongation time to produce a pre-rRNA unit. The diffusion length λ_{d} is estimated as $\sim 3\ \mu\mathrm{m}$ (see Table 1) and is larger

than the typical thickness, $\sim 200\,\mathrm{nm}$, of the DFC layer: the local equilibrium approximation is effective to treat the conformation of the pre-rRNAs in the DFC layer. The occupancy α_p, the volume fractions ϕ_p and ϕ_r of RBPs and nascent pre-rRNA, and the radius r_in thus turn over towards the minimum of the free energy, eq. 2.

Parameter	Meaning	Value	Ref.
b	Length of a RNA unit	$4\,\mathrm{nm} \approx 12\,\mathrm{b}$	22
η_w	Water viscosity	$1\,\mathrm{mPa}\cdot\mathrm{s}$	
v_e	Elongation rate	$6\,\mathrm{kb/min}$	23,24
T	Absolute Temperature	$300\,\mathrm{K}$	

Table 1 The values of the parameters used to estimate the diffusion length λ_d. The diffusion constant of a RNA unit is estimated as $D_r \sim \frac{k_\mathrm{B}T}{4\pi\eta_\mathrm{w}b} \sim 8\times10^{-11}\,\mathrm{m^2/s}$ and the time to synthesize a RNA unit is estimated as $\tau_\mathrm{s} = b/v_\mathrm{e} \sim 0.12\,\mathrm{s}$ by using the values listed in this table. We estimated b from the persistence length of single-stranded DNA.

Parameter estimate suggests that the terminal regions of nascent pre-rRNAs are highly stretched

The independent parameters involved in our theory and their estimates are summarized in Table 2. The kinetic constants involved in the Pol I transcription are included in ζ, see eq. 1. The energy gain due to the binding of RBPs to the pre-rRNA terminal regions is represented by $\epsilon k_\mathrm{B}T$. We represent the magnitudes of the multivalent interaction between RBPs by using the Flory interaction parameter χ. We neglect the dependence of the magnitudes of the interaction between RBPs on their binding state and also assume that solvent molecules and naked pre-rRNA units are equivalent in terms of the magnitudes of the interaction. This highlights the fact that the multivalent interaction between FBLs drives phase separation *in vitro*, not to lose the essence by introducing many interaction parameters. The volume fraction ϕ_p0 of RBPs in the nucleoplasm is taken into account via the chemical potential $\mu_\mathrm{p} = k_\mathrm{B}T\log\phi_\mathrm{p0}$.

The interaction parameter χ and the binding energy ϵ are important quantities of polymer physics, but are not experimentally well characterized. In the limit of vanishing

volume fraction of nascent RNAs, $\sigma_{\mathrm{in}} \to 0$, our model returns to the theory of the binary mixture of RBPs and solvent molecules (25), see eqs. 3 and 4. The latter theory predicts that the phase separation happens at the threshold interaction parameter χ_{tr0} $(= -\mu_{\mathrm{p}}/(k_{\mathrm{B}}T))$. FBL molecules show phase separation *in vitro* with the physiological concentration (10), implying that $\chi > \chi_{\mathrm{tr0}}$. If FBLs bind to the pre-rRNA terminal regions even in a dilute solution, it implies that $\epsilon > -\mu_{\mathrm{p}}/(k_{\mathrm{B}}T)$. The size of the FBL of the terminal region of a nascent pre-rRNA is $\approx 30\ \mathrm{nm}$ in the relaxed state ($\approx 130\ \mathrm{nm}$ in the maximally stretched state), while the thickness of a DFC layer is $\approx 100\ \mathrm{nm}$, implying that FBLs are highly stretched.

Parameter	Meaning	Estimate	Value	Ref
ζ	Rescaled pre-rRNA surface density	< 0.12	Varied	13
$\frac{\gamma_{\mathrm{p}} b^2}{N_r k_{\mathrm{B}} T}$	Rescaled surface tension per RBP	~ 0.03	0.03	
χ	Interaction parameter	> 10	12	
ϵ	RBP-RNA binding energy	> 10	-12	
$\mu_{\mathrm{p}}/(k_{\mathrm{B}}T)$	RBP chemical potential	-10	-10	10

Table 2 List of independent (dimensionless) parameters involved in our theory. Estimate of the unit length b of pre-rRNA and the absolute temperature are shown in Table 1. The surface density σ_{in} was estimated by the number of Pol I (50 Pol I per rDNA, 300 copies of active rDNA repeat per cell, ~ 10 FCs per nucleolus, ~ 2 nucleoli per cell) and the typical radius of FCs $r_{\mathrm{in}} \sim 100\ \mathrm{nm}$ (3,13). The surface tension γ_{p} can be estimated as $\sim k_{\mathrm{B}}T/b_{\mathrm{p}}^2$ (25,26), where the size b_{p} of FBL is $\approx 4\ \mathrm{nm}$ (27). The number of units N_{r} in the FBL-binding region of pre-rRNA is estimated by using its length $\sim 400\ \mathrm{b}$ (13). The chemical potential of FBL was estimated by using its concentration $\sim 1\ \mu\mathrm{M}$ (10).

The multivalent interaction between FBLs localizes these RBPs to the DFC layer and stretches the terminal regions of nascent pre-rRNAs

The occupancy α_{p}, the volume fractions ϕ_{p} and ϕ_{r} of RBPs and nascent pre-rRNA at the free energy minimum is derived by using the variational principle, see sec. S1B in the SI Appendix. For cases in which the curvature of the surfaces of FCs is not negligible,

α_{p}, ϕ_{p}, and ϕ_{r} are not uniform in the DFC layer. To avoid complexity arising from the geometry of the system, we first analyze the occupancy α_{p} and the volume fractions, ϕ_{p} and ϕ_{r}, in a DFC layer on a planer surface. This is indeed the limit of large FCs and the essential feature of the assembly of DFC layers is included in this analysis. In the planer geometry, the chemical potential of RBPs and the osmotic pressure is uniform in the DFC layer.

The magnitude of the multivalent interactions between RBPs (either bound to the pre-rRNA terminal regions or freely diffusing) increases with increasing the interaction parameter χ. Although it is not straightforward to experimentally control the interaction parameter χ of FBLs, it is instructive to analyze the composition of the layer occupied by the FBLs of nascent pre-rRNAs as a function of the interaction parameter χ, see Fig. 3. For cases in which the interaction parameter χ is small (which corresponds to self-association defective FBL ΔIDR mutant (13)), the major component of the layer is solvent (nucleoplasm), see the cyan line in Fig. 3. For $\chi < \chi_{\mathrm{s}}$, the excluded volume interaction between nascent pre-rRNA units dominates the attractive interaction between RBPs bound to these nascent pre-rRNAs (good solvent regime). The interaction parameter χ_{s} at the crossover is 2 in the limit of $\epsilon \ll \mu_{\mathrm{p}}/(k_{\mathrm{B}}T)$, such as the case of Fig. 3, see also eq. S31 in the SI Appendix for the general expression. The inverse of the volume fraction ϕ_{r} of nascent pre-rRNA is proportional to the extent of the stretching of the terminal regions of nascent pre-rRNAs. The terminal regions of these RNAs are somewhat stretched for $\chi \approx 0$ due to the excluded volume interaction between the pre-rRNA units (good solvent regime). The terminal regions shrink as the magnitude χ of the attractive interaction between RBPs bound to the terminal regions of nascent pre-rRNAs, see the green line in Fig. 3. For $\chi_{\mathrm{s}} < \chi < -\mu_{\mathrm{p}}/(k_{\mathrm{B}}T)$, the attractive interaction dominates the excluded volume interaction (poor solvent regime) and the terminal regions are collapsed with RBPs bound to these regions (melt regime), see the green line in Fig. 3.

At a threshold interaction parameter, $\chi_{\mathrm{th}} \approx -\mu_{\mathrm{p}}/(k_{\mathrm{B}}T)$, the volume fraction ϕ_{p} of freely diffusing RBPs jumps to a large value, see the magenta line in Fig. 3. In contrast, the volume fraction of the solvent (nucleosol) jumps to almost zero, see the cyan line in Fig. 3. The feature of the layer for $\chi > \chi_{\mathrm{th}}$ is analogous to the DFC layer observed experimentally (which we thus call DFC regime). The volume fraction ϕ_{r} of nascent pre-rRNA units jumps to a small value at $\chi \approx \chi_{\mathrm{th}}$, see the green line in Fig. 3, implying that the terminal regions of the nascent pre-rRNAs are stretched at the transition. Because the volume fraction ϕ_{r} is smaller than the case of $\chi = 0$, the stretching is not solely due to the fact that RBPs in the DFC layer behave as an athermal solvent to the RNP

complexes of RBPs and the pre-rRNA terminal regions. The terminal regions stretch so that the DFC layer can accommodate more RBPs to decrease the free energy due to the multivalent interactions between them. The stretching thus may be a transport mechanism of the ETS of pre-rRNAs towards the DFC layer.

The lateral pressure generated by nascent pre-rRNAs suppresses the growth of FCs

Now we discuss the DFC layers at the surfaces of spherical FCs to derive the radius of FCs in the steady state. The first (functional) derivatives of the free energy with respect to α_{p}, ϕ_{p}, and ϕ_{r} are zero in the steady state. In the spherical geometry, these conditions correspond to the fact that the chemical potential of RBPs and the chemical potential of pre-rRNA units, instead of the osmotic pressure, are uniform, see sec. S1B for the mathematics of the free energy minimization. We treat the DFC regime in which the volume fraction of solvent molecules is negligibly small and the occupancy α_{p} of the pre-rRNA terminal regions is approximately unity, see Table 2 and Fig. 3. We performed numerical and analytical calculations within these conditions, see sec. S3A in the SI Appendix.

In the spherical geometry, the volume fraction ϕ_{r} of pre-rRNA units is not uniform in the DFC layer and decreases with the distance r from the center ($r_{\mathrm{in}} < r < r_{\mathrm{ex}}$). It is because the elastic stress (proportional to the number of pre-rRNAs per unit area) generated by pre-rRNA decreases with increasing r, see the solid green line in Fig. 4. We performed the asymptotic analysis for $\phi_{\mathrm{r}} \ll 1$ by expanding the chemical potentials of proteins and pre-rRNA units in a power series and neglected higher order term of ϕ_{r}. This leads to an asymptotic expression, $\phi_{\mathrm{r}} \propto \frac{1}{r^2}$, which reasonably explains the numerical calculation, see the solid dark green line and broken light green line in Fig. 4 and also eq. S55 in the SI Appendix for the explicit form. The rest of the space in the DFC layer is filled by RBPs, see the inset of Fig. 4.

We used the profile of the pre-rRNA units to derive the free energy as a function of the radius r_{in} of FCs. For cases in which the Pol I transcription is inhibited, the free energy of the system is a monotonically decreasing function of the radius r_{in}, implying that, the radius of FCs increases with time by coarsening or coalescence. For cases in which the Pol I transcription is active, the free energy generated by the terminal regions of the nascent pre-rRNA is an intriguing function of r_{in}, which has a minimum, see the solid black line in Fig. 5A. Indeed, the surface free energy, the second and third terms of eq.

2, is not significant for the values of parameters estimated in Table 2, see the broken cyan line in Fig. 5A. In such case, the free energy is simpler if it is shown as a function of the ratio $r_{\mathrm{ex}}/r_{\mathrm{in}}$, see Fig. 5B and eq. S59 in the SI Appendix.

The first derivative of the free energy with respect to the radius r_{in} is zero at the minimum of the free energy,

$$\Delta\Pi_{\parallel} \approx \gamma_{\mathrm{in}} + \gamma_{\mathrm{ex}} \frac{r_{\mathrm{ex}}^2}{r_{\mathrm{in}}^2}. \qquad [3]$$

Eq. 3 represents the surface tensions, γ_{in} and γ_{ex}, are balanced to the lateral osmotic pressure $\Delta\Pi_{\parallel}$ generated in the DFC layer (the complete form is shown in eq. 21). The radius r_{in} at the minimum of the free energy decreases with increasing the transcription level, see Fig. 6. The radius r_{in} at the minimum of the free energy has an asymptotic form

$$\frac{r_{\mathrm{in}}}{bN_{\mathrm{r}}} = \frac{2}{\sqrt{3}}\left(\chi + \frac{\mu_{\mathrm{p}}}{k_{\mathrm{B}}T}\right)^{\frac{1}{2}} \zeta^{-\frac{1}{2}}, \qquad [4]$$

see also the broken line in Fig. 6. Eq. 4 is derived by expanding the free energy in a power series of ϕ_{r} and by using the asymptotic form of ϕ_{r}, see sec. S3A in the SI Appendix for the details of the derivation. We also neglected the surface free energy, the second and third terms of eq. 2, because it is not significant with our estimate in Table 2. Our theory therefore predicts that the radius of FCs decreases with the inverse of the square root of the transcription rate. At the minimum of the free energy, the ratio of the radii is $\frac{r_{\mathrm{ex}}}{r_{\mathrm{in}}} \approx 2$, which roughly agrees with the fact that the radius of FCs and the thickness of DFC layers are the same order of length scales, $\propto 100\ \mathrm{nm}$, see Fig. 5B.

Mild inhibition of Pol I increases the size of FCs

The main prediction from our theoretical model is that the size of FCs increases by reducing the expression level of nascent pre-rRNAs. To experimentally test this prediction, we used BMH-21 and CX-5461, specific Pol I inhibitors, which reduce nascent pre-rRNA levels in a dose-dependent manner (28,29) (Fig. S1A and B). In untreated cells, small foci of UBF (a marker for FCs) and FBL (a marker for DFC) proteins were dispersed within the nucleoli as previously reported (11) (Figs. 7A, S2A, S2B, and S3A). In contrast, UBF and FBL proteins were relocalized to nucleolar caps in the presence of high doses

of BMH-21 (0.5 μM) or CX-5461 (2 μM), as reported (11,28) (Figs. 7A, S2A, S2B, and S3A). Strikingly, the FCs were larger in cells treated with the medium doses of BMH-21 (0.0625, 0.125, and 0.25 μM) or CX-5461 (0.25, 0.5, and 1 μM) than in untreated cells (Figs. 7A, S2A, S2B, and S3A). We then quantified the size of the FCs under these untreated and mildly treated conditions (Figs. 7B, 7C, S3B, S3C, and S4). Indeed, the longest axis (Lx) and area of the FCs increase with increasing the dose of BMH-21 and CX-5461. As theoretically predicted, the Lx and area of the FCs increase according to pre-rRNA level reduction (Figs. 7D, 7E, S3D, and S3E).

FC radius is a power function of the pre-rRNA transcription level with an exponent of approximately -0.5

To compare our theory and experiments more quantitatively, we curve-fit the square root of the area of FCs as a function of the transcription level by a power function (Fig. 8). The scaling exponent that describes the dependence of the square root of the area of FCs on the transcription level is a universal quantity that does not depend on specific values of the parameters. Checking such scaling exponents with experiments is the first thing to do to test theories in polymer physics (30). By fitting the data with a power function, we found that the scaling exponent is -0.49 for the case of the BMH-21 treatment, -0.46 for the case of the CX-5461, and -0.48 if both data are fitted. The scaling exponent predicted by our theory -0.5 reasonably agrees with our experiments, see eq. 4.

DISCUSSION

Our theory predicts that the terminal regions of nascent pre-rRNAs at the surfaces of FC microphases in a nucleolus generate the lateral osmotic pressure and suppress the growth of microphases. Our theory predicts that the radius of FCs is proportional to the inverse of the square root of the transcription rate. This prediction is consistent with our experiments. The parameter ζ is also proportional to the inverse of the rate τ_{pr}^{-1} of co-transcriptional processing that cleaves the terminal regions of pre-rRNA. Our theory thus predicts that the radius of FCs is proportional to the square root of the processing rate τ_{pr}^{-1}. The inhibition of processing induced by ribosomal protein depletion, such as uL18 (RPL5) and uL5 (RPL11), changes the multiphase structure of nucleoli (31). Indeed, recent experiments have demonstrated that long pre-rRNAs are accumulated in RPL5 knockdown cells and the size of FCs in such cells is smaller than that in the wild type (32). The consistency between our theory and experiments suggests that the growth of FCs is suppressed by the terminal regions of nascent pre-rRNAs localized at the

375 surfaces of FCs. This implies that the elastic energy of the terminal region is the driving
376 force of the transport of the 5' ETSs cleaved by RNA processing towards GC.

377 In many cases, the multivalent interaction between complexes of RNA and RBPs drives
378 the growth of condensates (33,34) (Fig. 8A). The size of such condensates increases
379 with increasing the transcription rate (14,17,35). In contrast, for the case of FCs in
380 nucleoli, the multivalent interaction between the complexes of nascent RNA and RBPs
381 rather suppresses the growth of FCs (11). The size of FCs indeed decreases with
382 increasing the transcription rate. Our theory predicts that the suppression of the growth
383 of FCs by transcription results from the fact that pre-rRNAs are end-grafted to the
384 surfaces of FCs via Pol I (Fig. 8B).

385 Our theory predicts that the function of the terminal regions of nascent pre-rRNAs is
386 analogous to surfactants, such as lipids. If the surfactants at an interface between two
387 immiscible liquids are dense enough to form a monomolecular liquid film, these
388 surfactants decrease the interfacial tension to almost zero to disperse multiple droplets
389 even in the thermodynamic equilibrium (microemulsion) (25,36). The surfactant
390 monolayer acts as a kinetic barrier to suppress the coalescence and decreases the
391 hydrostatic pressure of the droplet to suppress the coarsening (9,25). These features are
392 analogous to the terminal regions of pre-rRNAs at the surfaces of FCs. The fact that
393 some RNAs and proteins can act as surfactants was discussed in recent researches
394 (37,38). There are also differences between nascent pre-rRNA and surfactants. First and
395 foremost, surfactants are localized at interfaces at the thermodynamic equilibrium, while
396 the terminal regions of nascent pre-rRNAs are localized at the FC-DFC interfaces only
397 during the transcription and their surface activity is regulated by Pol I transcription
398 dynamics. Second, the hydrophobic chains of surfactants in a liquid monolayer tend to
399 form a melt, while the terminal regions of pre-rRNA are extended due to the RBPs freely
400 diffusing in the DFC layers. Last, but not least, surfactants can freely diffuse in a
401 monolayer, while the terminal regions of nascent pre-rRNAs are anchored to the rDNA
402 at the interface via Pol I and thus are not mobile.

403 In our model, we focused on FBLs because these RBPs contribute most significantly to
404 the localization of the terminal regions of pre-rRNAs to the DFC layer (13). FRAP
405 experiments on the condensates of FBLs reconstituted *in vitro* suggest that these
406 condensates are thixotropic (and probably also be viscoelastic) and become gels in a
407 long timescale (10). Indeed, recent experiments showed that long non-coding RNA
408 SLERT facilitates the transition of the RNA helicase DDX21 to the closed conformation

and ensures the fluidity of proteins in the DFC layer (39). This mechanism ensures the validity of our assumption that unbound FBLs can diffuse freely in the DFC layer, although we did not take into account these factors explicitly.

Although our theory probably could capture the essential features that are necessary to understand the assembly mechanism of the multiphase structure of nucleolus, it is not complete. First, the layers at the interface between FCs and GC are not uniform, but DFC regions are flanked by the regions, in which FBLs are not observed by super-resolution microscopy and are not visible by electron microscopy. Second, we did not take into account the downstream pre-rRNA regions that are not bound by FBLs. These downstream regions were observed at the surfaces of FCs (13). The direct contribution of rDNAs localized at the surfaces of FCs are not significant, see S4 in the SI Appendix. Third, we did not explicitly take into account the transport dynamics of pre-rRNAs in GCs. Fourth, RNAs can be not only cleaved, but also can be folded and/or chemically modified during the co-transcriptional processing. The processing of pre-rRNAs in yeast has been well-documented (40,41), but much less in higher eukaryotes (42,43), in which the multiphase structure of nucleolus is usually observed. It is of interest to understand the mechanism of the processed pre-rRNAs, which have the affinity to FCs, penetrate through the DFC layer towards the GC. One possible hypothesis is that the processed pre-rRNAs pass the flanking regions of the DFC layer. These flanking regions increase the density of the terminal regions of pre-rRNAs in the DFC compartments and enhance the lateral osmotic pressure. The enhanced lateral pressure and/or the kinetic trapping of the coalescence of FCs by nascent pre-rRNAs may explain the fact that the radius of FCs observed in experiments is smaller than that predicted by our theory. Whether the multiphase structure of the nucleolus contributes to its function is not yet clear. It is of interest to extend our theory to understand the structure-function relationship of the nucleolus (44). However, following the approach of the classical theoretical physics, our present theory should be experimentally tested before adding more assumptions that have not been experimentally explored.

The key assumption of our theory is that the terminal regions of nascent pre-rRNAs span between the top to the bottom of the DFC layer. This is motivated by a recent experiment that the upstream half of ETSs are localized at the DFC layer and the downstream half is localized at the FC (13). The stretching of the terminal regions results from the multivalent interactions between FBLs and thus our theory should be tested in the condition of high FBL volume fraction. In the conventional picture, the DFC layer is composed of 5’ ETSs that are already cleaved and folded by RNA processing. Such

diffusive molecules tend to make the interaction between condensates attractive (the depletion interaction) (25), however, the non-equilibrium nature of the transcription may change the situation. We envisage a future theoretical study to predict the stable size of FCs with the conventional picture to check if the latter agrees with existing experiments, including ours.

Our theory may provide insight into the size control mechanism of other nuclear bodies. The size of nuclear speckles (5) increases by the suppression of transcription. The stability of transcriptional condensate depends on the frequency of transcription and the length of transcripts (45,46). Transcriptional condensates are actively studied in recent experiments (45-49). The simulations by Henninger and coworkers predict that RNAs diffuse freely in the interior of condensates and destabilize the condensates due to the electrostatic repulsion (45). In contrast, Hilbert and coworkers argued that DNA-Pol II-RNA complexes are localized at the interface between transcriptional condensates (rich in RNA and proteins) and the exterior (rich in DNA) and act as surfactants that suppress the coalescence and coarsening of the condensates (46), analogous to microemulsion (see above). Our theory is somewhat similar to the idea of Hilbert and coworkers, but different in the fact that the complexes of nascent pre-rRNAs and RBPs form distinct phase at the interface between FCs and GC due to the transcription and FCs and GC are somewhat similar in terms of the relative affinity to the nucleoplasm, as characterized by the interfacial tension (10). The Pol II transcription is regulated by the phosphorylation of the C-terminal domains and is somewhat different from the Pol I transcription. It is of interest to take into account such differences in an extension of our present theory to understand the assembly mechanism of nuclear bodies and their functions.

The multiphase structure of nucleoli may be somewhat analogous to that observed in nuclear stress bodies (nSBs) by electron microscopy (50). nSBs are assembled during the thermal stress condition and are composed of HSATIII architectural RNA and specific RBPs (51). HSATIII is transcribed by Pol II from the pericentromeric Satellite III regions, which are enriched in tandem repeats (52,53). These features common with nucleoli motivate us to think of a general mechanism involved in the assembly of the multiple subcompartments. The nascent RNAs, which are produced by transcription and are modulated by RNA processing, are important elements that regulate the multiphase structures, and possibly their functions, of nuclear bodies.

MATERIALS AND METHODS

Transcription and RNA processing

The occupancy n_{ps} of the TSS of the active rDNA by Pol I follows the kinetic equation

$$\frac{d}{dt}n_{\mathrm{ps}} = k_{\mathrm{on}}\rho(1 - n_{\mathrm{ps}}) - k_{\mathrm{off}}n_{\mathrm{ps}} - k_{\mathrm{e}}n_{\mathrm{ps}}. \quad [6]$$

Eq. 6 suggests that the occupancy n_{ps} changes due to the binding of Pol I from the FC (the first term), the unbinding of Pol I from the TSS to the FC without starting transcription (the second term), and the initiation of the elongation of Pol I (the third term), see Fig. 2A. k_{on} is the rate constant for the binding of Pol I to TSS and ρ is the concentration of Pol I in a FC (which will be determined later). k_{off} is the rate constant for the unbinding of Pol I from TSS. k_{e} is the rate of the transition of Pol I from the bound state to the elongation state.

The number n_{pe} of elongating Pol I protein complexes with pre-processed nascent pre-rRNA follows the kinetic equation

$$\frac{d}{dt}n_{\mathrm{pe}} = k_{\mathrm{e}}n_{\mathrm{ps}} - \frac{n_{\mathrm{pe}}}{\tau_{\mathrm{pr}}}. \quad [7]$$

Eq. 7 suggests that the number n_{pe} changes due to the release of Pol I from TSS for elongation (the first term) and the cleavage of the FBL-binding terminal region of nascent pre-rRNA (the second term), see Fig. 2B. τ_{pr} is the average time between the transcription initiation and the cleavage of the terminal regions of the pre-rRNA.

The number n_{p0} of elongating Pol I with processed nascent pre-rRNA follows the kinetic equation

$$\frac{d}{dt}n_{\mathrm{p0}} = \frac{n_{\mathrm{pe}}}{\tau_{\mathrm{pr}}} - \frac{n_{\mathrm{p0}}}{\tau_0}. \quad [8]$$

Eq. 8 suggest that the number n_{p0} changes due to the the cleavage of the terminal regions of pre-rRNAs (the first term) and the transcription termination (the second term), see Fig. 2C. τ_0 is the average time between the cleavage of FBL-binding region and the transcription termination.

The numbers, n_{ps}, n_{pe}, and n_{p0}, of Pol I in each state are derived for the steady state, $\frac{dn_{\mathrm{ps}}}{dt} = \frac{dn_{\mathrm{pe}}}{dt} = \frac{dn_{\mathrm{p0}}}{dt} = 0$, by using eqs. 6-8. The inverse time k_{e} of the transcription initiation is much smaller than the inverse k_{off} of the unbinding of Pol I from TSS, $k_{\mathrm{e}} \ll$

k_{off}. The concentration ρ of Pol I in a FC is determined by the condition

$$(n_{\mathrm{ps}} + n_{\mathrm{pe}} + n_{\mathrm{p0}})N_{\mathrm{a}} + \rho V_{\mathrm{m}} = N_{\mathrm{pol}} \qquad [9]$$

that the sum of the number of Pol I during transcription (the first term) and the number of Pol I diffusing in microphases (the second term) in the system is constant. All the parameters involved in eq. 9 do not depend on the size of FCs, see eqs. 6-8. The concentration ρ of Pol I in FCs thus does not depend on the size of FCs.

The surface density σ_{in} of the FBL-binding terminal regions of nascent pre-rRNAs at each FC (the number of nascent pre-rRNAs per unit area of each FC surface) is represented as

$$\sigma_{\mathrm{in}} = \frac{n_{\mathrm{pe}}}{4\pi r_{\mathrm{in}}^2}\left(\frac{4\pi r_{\mathrm{in}}^3}{3V_{\mathrm{m}}}N_{\mathrm{a}}\right) = \frac{1}{3}k_{\mathrm{e}}\tau_{\mathrm{pr}}\frac{\rho}{\rho + K_{\mathrm{pl}}}\frac{N_{\mathrm{a}}}{V_{\mathrm{m}}}r_{\mathrm{in}}. \qquad [10]$$

by assuming that the terminal regions of nascent pre-rRNA is distributed uniformly at the surfaces of FCs. We note that $3V_{\mathrm{m}}/(4\pi r_{\mathrm{in}}^3)$ is the number of FCs in a nucleolus. The last form of eq. 10 is derived by using the solution of eqs. 6-8.

Thickness of DFC layer

The exterior radius r_{ex} (see also Fig. 1B) is determined by the relationship

$$\int_{r_{\mathrm{in}}}^{r_{\mathrm{ex}}} dr 4\pi r^2 \phi_{\mathrm{r}} = 4\pi r_{\mathrm{in}}^2 \sigma_{\mathrm{in}} N_{\mathrm{r}}\,, \qquad [11]$$

where N_{r} is the average number of units in the terminal region of a nascent pre-rRNA. It is a mean field treatment that assumes that nascent RNAs are composed of the same number of units and is effective within the Alexander-de Gennes approximation, with which the brush height is determined by the distance between neighboring grafting points and the average number of units per chain (if one neglects the fact that the lateral fluctuations of a chain composed of N_{r} units is limited to $\sim N_{\mathrm{r}}^{1/2}b$) (21, 54).

Free energy of DFC layer

The free energy of each DFC layer has the form

$$F_{\mathrm{d}} = \int_{r_{\mathrm{in}}}^{r_{\mathrm{ex}}} dr \frac{4\pi r^2}{b^3} f_{\mathrm{d}} \qquad [12]$$

with

$$f_{\mathrm{d}} = f_{\mathrm{ela}} + f_{\mathrm{mix}} + f_{\mathrm{int}} + f_{\mathrm{bnd}} - \mu_{\mathrm{p}}(\phi_{\mathrm{p}} + \alpha_{\mathrm{p}}\phi_{\mathrm{r}}) + \Pi_{\mathrm{ex}} b^3. \qquad [13]$$

Eq. 12 is the functional of the local volume fraction ϕ_{r} of nascent pre-rRNA units, the local volume fraction ϕ_{p} of RBPs, and the occupancy α_{p} of nascent pre-rRNA units by RBPs, which are functions of the distance r from the center of the FC ($r_{\mathrm{in}} < r < r_{\mathrm{ex}}$), see Fig. 1B. b is the length of a pre-rRNA unit. This free energy is composed of 4 contributions: f_{ela} is the elastic free energy density of the terminal regions of nascent RNAs, f_{mix} is the free energy density due to the mixing entropy of RBPs and solvent molecules, f_{int} is the free energy density due to the interactions between RBPs, and f_{bnd} is the free energy density due to the binding of RBPs to the terminal regions of nascent RNAs. μ_{p} is the chemical potential of RBPs and Π_{ex} is the osmotic pressure from the exterior.

The (entropic) elastic free energy density has the form

$$\frac{f_{\mathrm{ela}}}{k_{\mathrm{B}}T} = \frac{3}{2}\frac{b^4\sigma^2(r)}{\phi_{\mathrm{r}}}, \qquad [14]$$

where $\sigma(r)$ is the surface density of FBL-binding regions of nascent pre-rRNAs. $\sigma(r) = \sigma_{\mathrm{in}} r_{\mathrm{in}}^2/r^2$ for cases in which the surface of FCs is sphere and $\sigma(r) = \sigma_{\mathrm{in}}$ for cases in which the surface of FCs is planer (which corresponds to the limit of $\frac{r_{\mathrm{ex}}-r_{\mathrm{in}}}{r_{\mathrm{in}}} \ll 1$). The volume fraction ϕ_{r} of pre-rRNA units decreases as the terminal regions of the nascent pre-rRNAs are stretched. Eq. 14 represents the fact that the elastic free energy f_{ela} increases as these terminal regions are stretched. Eq. 14 takes into account the spherical geometry of the system in an extension of the Alexander model (that assumes that the concentration of the terminal regions of nascent pre-rRNA is uniform in the DFC layer in the limit of $\frac{r_{\mathrm{ex}}-r_{\mathrm{in}}}{r_{\mathrm{in}}} \ll 1$) in the spirit of the Daoud-Cotton theory (55), see sec. S5 in the SI Appendix for the derivation. k_{B} is the Boltzmann constant and T is the absolute temperature.

The free energy due to the mixing entropy of RBPs and solvent molecules has the form

$$\frac{f_{\mathrm{mix}}}{k_{\mathrm{B}}T} = \phi_{\mathrm{p}} \log \phi_{\mathrm{p}} + \left(1 - \phi_{\mathrm{p}} - (1+\alpha_{\mathrm{p}})\phi_{\mathrm{r}}\right) \log\left(1 - \phi_{\mathrm{p}} - (1+\alpha_{\mathrm{p}})\phi_{\mathrm{r}}\right). \qquad [15]$$

The mixing free energy, eq. 15, has the contributions of the mixing entropy of RBPs (the

first term) and the mixing entropy of solvent molecules (the second term).

The free energy due to the interactions between RBPs has the form

$$\frac{f_{\mathrm{int}}}{k_{\mathrm{B}}T} = -\chi\left(\phi_{\mathrm{p}} + \alpha_{\mathrm{p}}\phi_{\mathrm{r}}\right)^2, \qquad [16]$$

where χ is the interaction parameter that accounts for the attractive interactions. For simplicity, we assumed that RBPs bound to the terminal regions of nascent pre-rRNAs are equivalent to RBPs freely diffusing in the DFC layer and that solvent molecules are equivalent to nascent RNA units in terms of the interactions, see also the discussion in Parameter estimate.

The free energy due to the binding of RBPs to nascent RNAs has the form

$$\frac{f_{\mathrm{bnd}}}{k_{\mathrm{B}}T} = \phi_{\mathrm{r}}\left[\alpha_{\mathrm{p}}\log\alpha_{\mathrm{p}} + \left(1-\alpha_{\mathrm{p}}\right)\log\left(1-\alpha_{\mathrm{p}}\right) + \epsilon\alpha_{\mathrm{p}}\right], \qquad [17]$$

where $\epsilon k_{\mathrm{B}}T$ is the energy increase due to the binding of RBPs to nascent RNAs. For simplicity, we assumed that each nascent RNA unit has one binding site of RBPs.

Free energy of system

The free energy F of the system, eq. 2 is derived by using the fact that the number of microphases in the system is $3V_{\mathrm{m}}/(4\pi r_{\mathrm{in}}^3)$ to derive this form. The interfacial tension between GC and nucleosol is relative small (3,10) and FC is excluded out from the nucleolus by the transcription inhibition (3,11), implying that the interfacial tension between FC and nucleosol is even smaller. In vitro experiments suggest that the attractive interaction between FBLs is much larger than that between nucleophosmins, a major component of GC (10). It implies that the interfacial tension between DFC and GC and that between DFC and FC are larger than their difference. By neglecting the difference between these interfacial tensions, the interfacial tensions γ_{in} and γ_{ex} at the interior and the exterior interfaces are represented by the forms

$$\gamma_{\mathrm{in}} = \gamma_{\mathrm{p}}\left(\phi_{\mathrm{p}}(r_{\mathrm{in}}) + \alpha_{\mathrm{p}}(r_{\mathrm{in}})\phi_{\mathrm{r}}(r_{\mathrm{in}})\right) \qquad [18]$$

$$\gamma_{\mathrm{ex}} = \gamma_{\mathrm{p}}\left(\phi_{\mathrm{p}}(r_{\mathrm{ex}}) + \alpha_{\mathrm{p}}(r_{\mathrm{ex}})\phi_{\mathrm{r}}(r_{\mathrm{ex}})\right) \qquad [19]$$

where γ_{p} is the surface tension between a nucleosol and a liquid of the RBPs and is proportional to χ.

Lateral osmotic pressure

The lateral osmotic pressure $\Pi_{\parallel}$ can be defined by

$$\Delta\Pi_{\parallel} = \sigma_{\mathrm{in}}^{2} \frac{\partial}{\partial \sigma_{\mathrm{in}}} \left(\frac{F_{\mathrm{d}}}{4\pi r_{\mathrm{in}}^{2} \sigma_{\mathrm{in}}} \right), \qquad [20]$$

where the derivative with respect to σ_0 is taken with the condition that $4\pi\sigma_{\mathrm{in}} r_{\mathrm{in}}^{2}$ is constant (this increases the area of the surface of a FC without changing the composition of the DFC layer). $\Delta\Pi_{\parallel}$ is the lateral osmotic pressure, from which the contribution of the isotropic osmotic pressure is subtracted.

Radius of FCs at free energy minimum

The free energy, eq. 1, is represented as a function only of the radius r_{in} of FCs if the occupancy, α_{p}, and the volume fractions, ϕ_{p} and ϕ_{r}, derived by using eqs. 2-5 are substituted into eq. 1. The radius r_{in} at the steady sate is derived by the condition $\frac{dF}{dr_{\mathrm{in}}} = 0$ with the condition that $\sigma_0 \propto r_{\mathrm{in}}$ (this increases the area of the surfaces of FCs with the optimization of the arrangement of the active rDNA repeats). This leads to the form

$$\Delta\Pi_{\parallel} - \left(\gamma_{\mathrm{in}} + \gamma_{\mathrm{ex}} \frac{r_{\mathrm{ex}}^{2}}{r_{\mathrm{in}}^{2}} \right) + r_{\mathrm{in}} \left(\frac{\partial \gamma_{\mathrm{in}}}{\partial r_{\mathrm{in}}} + \frac{\partial \gamma_{\mathrm{ex}}}{\partial r_{\mathrm{in}}} \frac{r_{\mathrm{ex}}^{2}}{r_{\mathrm{in}}^{2}} \right) = 0, \qquad [21]$$

which represent the fact that the surface tension is balanced to the surface pressure generated by the FBRs of nascent pre-rRNAs.

Cell culture, drug treatment, reverse transcription-quantitative PCR (RT-qPCR), immunofluorescence, and quantification of the size of FCs

HeLa cells were maintained in DMEM containing high glucose (Nacalai Tesque, Cat# 08458-16) supplemented with 10% FBS (Sigma) and Penicillin-Streptomycin (Nacalai Tesque). Cells were treated with BMH-21 (Selleckchem, Cat# S7718) or CX-5461 (AdooQ Bioscience) for 3 hours. Quantification of nascent pre-rRNAs (forward primer: 5'-CCTTCCCCAGGCGTCCCTCG-3', reverse primer: 5'-GGCAGCGCTACCATAACGGA-3') (11) by RT-qPCR was performed using LightCycler 480 II (Roche). GAPDH mRNAs were used as a loading control (14). The antibodies to

609 UBF (Santacruz, F-9, sc-13125, mouse monoclonal antibody, 1:50 dilution), FBL
610 (Proteintech, 16021-1-AP, rabbit polyclonal antibody, 1:500 dilution), and
611 NPM1/Nucleophosmin (Abcam, ab183340, SP236, rabbit polyclonal antibody, 1:100
612 dilution) were used to visualize FCs, DFCs, and GCs in immunofluorescence,
613 respectively. Cells were grown on coverslips (Matsunami; 18 mm round) and fixed with
614 4% paraformaldehyde/PBS at room temperature for 10 min. Then, the cells were washed
615 three times with 1 x PBS, permeabilized with 0.5% Triton-X100/PBS at room temperature
616 for 5 min, and washed three times with 1 x PBS. The cells were incubated with 1 x
617 blocking solution (Roche, Blocking reagent and TBST [1 x TBS containing 0.1% Tween
618 20]) at room temperature for 1 hour. Then, the coverslips were incubated with primary
619 antibodies in 1 x blocking solution at room temperature for 1 hour, washed three times
620 with TBST for 5 min, incubated with secondary antibodies (anti-mouse IgG, Alexa Fluor
621 488, superclonal [Thermo Fisher Scientific, Cat#A28175], anti-rabbit IgG, Alexa Fluor
622 568 [Thermo Fisher Scientific, Cat#A11036]) at room temperature for 1 hour, and washed
623 three times with TBST for 5 min. The coverslips were mounted with a Vectashiled hard
624 set mounting medium with DAPI (Vector, H-1500). Super-resolution images were
625 acquired using ZEISS LSM900 with Airyscan 2. Quantification of the FCs marked by UBF
626 staining within the nucleoli labeled by NPM1 staining was performed using NIS Elements
627 Advanced Research (NIKON). “FillArea” and “MaxFeret” of the UBF foci (FCs) detected
628 with an intensity threshold were quantified as area and Lx of the FCs (Fig. S4).

629 **DATA AVAILABILITY**

630 Mathematica file used for the numerical calculations are available in figshare with the
631 identier (https://doi.org/10.6084/m9.figshare.16599446).

632 **ACKNOWLEDGMENT**

633 This research was supported by KAKENHI grants from the Ministry of Education, Culture,
634 Sports, Science, and Technology (MEXT) of Japan [to T. Yamamoto (20H05934,
635 21K03479, 21H00241), T. Yamazaki (21H00253, 22H02545), KN (19K06478,
636 22K06083),and TH (20H00448, 20H05377,21H05276)], JST, PRESTO Grant Number
637 JPMJPR18KA (to T. Yamamoto), the Mochida Memorial Foundation for Medical and
638 Pharmaceutical Research (to T. Yamazaki), the Naito Foundation (to T. Yamazaki), the
639 Takeda Science Foundation (to T. Yamazaki), and JST CREST Grant Number
640 JPMJCR20E6 (to T.H.). T. Yamazaki thanks Toyofumi Kameoka (NIKON SOLUTIONS
641 CO., LTD.) and Takayuki Funato (NIKON SOLUTIONS CO., LTD.) for support of
642 microscopic image analyses. T. Yamamoto acknowledges the fruitful discussion with

Noriko Saito (Japanese Foundation for Cancer Research), Yuma Ito (Tokyo Institute of Technology), Satoru Ide (National Institute of Genetics), Tsutomu Suzuki (Univ. of Tokyo), Takahiko Kobayashi (Univ. of Tokyo), Yutetsu Kuruma (JAMSTEC), Shintaro Iwasaki (Univ. of Tokyo), Sumio Sugano (Chiba University), Haruhiko Siomi (Keio Univ.), Hideaki Matsubayashi (Johns Hopkins Univ.), and Naomichi Takemata (Kyoto Univ.).

REFERENCE

1. S Klinge, J Woolford Jr, Ribosome assembly coming into focus. *Nat. Rev. Mol. Cell Biol.* **20,** 116–131 (2019).

2. B McStay, I Grummt, The Epigenetics of rRNA genes: From Molecular to Chromosome Biology. *Annu. Rev. Cell Dev. Biol.* **24,** 131–157 (2008).

3. D Lafontaine, J Riback, R Bascetin, C Brangwynne, The nucleolus as a multiphase liquid condensate. *Nat. Rev. Mol. Cell Biol.* **22,** 165–182 (2021).

4. J Berry, S Weber, N Vaidya, M Haataja, C Brangwynne, RNA transcription modulates phase transition driven nuclear body assembly. *Proc. Natl. Acad. Sci. USA* **112,** E5237–E5245 (2015).

5. A Lamond, D Spector, Nuclear speckles: a model for nuclear organelles. *Nat. Rev. Mol. Cell Biol.* **4,** 605–612 (2003).

6. S Nakagawa, T Yamazaki, T Hirose, Molecular dissection of nuclear paraspeckles: towards understanding the emerging world of the RNP milieu. *Open Biol.* **8,** 180150 (2018).

7. T Chujo, T Yamazaki, T Hirose, Architectural RNA (arcRNAs): A class of long noncoding RNAs that function as the scaffold of nuclear bodies. *Biochim. Biophys. Acta* **1859,** 139–146 (2015).

8. T Yamazaki, S Nakagawa, T Hirose, Architectural RNAs for Membraneless Nuclear Body Formation. *Cold Spring Harb. Symp. Quant. Biol.* **84,** 227–237 (2019).

9. M Doi, *Soft Matter Physics.* (Oxford University Press, Oxford, UK.), (2013).

10. M Feric, et al., Coexisting Liquid Phases Underlie Nucleolar Subcompartments. *Cell* **165,** 1686–1697 (2016).

671 11. S Ide, R Imai, H Ochi, K Maeshima, Transcriptional suppression of ribosomal DNA
672 with phase separation. *Sci. Adv.* **6,** eabb5953 (2020).

673 12. A Maiser, et al., Super-resolution in situ analysis of active ribosomal DNA chromatin
674 organization in the nucleolus. *Sci. Rep.* **10,** 7462 (2020).

675 13. R Yao, et al., Nascent Pre-rRNA Sorting via Phase Separation Drives the Assembly
676 of Dense Fibrillar Components in the Human Nucleolus. *Mol. Cell* **76,** 767–783 (2019).

677 14. T Yamazaki, et al., Paraspeckles are constructed as block copolymer micelles.
678 *EMBO J* **40,** e107270 (2021).

679 15. S Souquere, G Beauclair, F Harper, A Fox, G Pierron, Highly Ordered Spatial
680 Organization of the Structural Long Noncoding Neat1 RNAs Within Paraspeckle Nuclear
681 Bodies. *Mol. Biol. Cell* **21,** 4020–4027 (2010).

682 16. J West, et al., Structural, super-resolution microscopy analysis of paraspeckle
683 nuclear body organization. *J. Cell Biol.* **214,** 817–830 (2016).

684 17. T Yamamoto, T Yamazaki, T Hirose, Triblock copolymer micelle model of spherical
685 paraspeckles. *Front. Mol. Biosci.* **9,** 925058 (2022).

686 18. T Hirose, et al., NEAT1 long noncoding RNA regulates transcription via protein
687 sequestration within subnuclear bodies. *Mol. Biol. Cell* **25,** 169–183 (2014).

688 19. P Tchelidze, A Benassarou, H Kaplan, MF O'Donohue, L Lucas, C Terryn, L Rusishvili,
689 G Mosidze, N Lalun D. Ploton, Nucleolar sub-compartments in motion during rRNA
690 synthesis inhibition: Contraction of nucleolar condensed chromatin and gathering of
691 fibrillar centers are concomitant. PLOS ONE **12,** e0187977 (2017).

692 20. T Stasevich, et al., Regulation of RNA polymerase II activation by histone acetylation
693 in single living cells. *Nature* **516,** 272–275 (2014).

694 21. S Alexander, Adsorption of chain molecules with a polar head a scaling description.
695 *J. Phys. France* **38,** 983–987 (1980).

696 22. E Roth, A G Azaria, O Girshevitz, A Bitler, and Y Garini, Measuring the conformation
697 and persistence length of single-strand DNA using a DNA origami structure. *Nano Lett.*
698 **18,** 6703-6709.

699 23. M Dundr, U Hoffmann-Rohrer, Q Hu, I Grummt, L I Rothblum, R D Phair, and T Misteli,
700 Mammalian RNA Polymerase in Vivo. *Science* **298,** 1623-1626 (2002).

701 24. V Stefanovsky, F Langlois, T Gagnon-Kugler, L I Rothblum, and T Moss, Growth
702 factor signaling regulates elongation of RNA polymerase I transcription in mammals via
703 UBF phosphorylation and r-chromatin remodeling. *Mol Cell* **21,** 629-639.

704 25. S Safran, *Statistical Thermodynamics of Surfaces, Interfaces, and Membranes.*
705 (Westview Press, CO, US.), (2003).

706 26. P G de Gennes, F Brochard-Wyart, and D Quéré, Wetting phenomena Drops,
707 Bubbles, Pearls, Waves. (Springer, NY, US.) (2004).

708 27. H Wang, D Boisvert, K K Kim, R Kim, and S H Kim, Crystal structure of a fibrillarin
709 homologue from Methanococcus jannaschii, a hyperthermophile, at 1.6 Å resolution.
710 *EMBO J.* **19,** 317-323 (2000).

711 28. K Peltonen, et al., A Targeting Modality for Destruction of RNA Polymerase I that
712 Possesses Anticancer Activity. *Cancer Cell* **25,** 77–90 (2014).

713 29. D Drygin, et al., Targeting RNA Polymerase I with an Oral Small Molecule CX-5461
714 Inhibits Ribosomal RNA Synthesis and Solid Tumor Growth. *Cancer Res.* **71,** 1418-1430
715 (2011).

716 30. P de Gennes, *Scaling Concepts in Polymer Physics*. (Cornell Univ. Press, NY, US.),
717 (1979).

718 31. E Nicolas, et al., Involvement of human ribosomal proteins in nucleolar structure and
719 p53-dependent nucleolar stress. *Nat. Comm.* **7,** 11390 (2016).

720 32. H Matsumori, et al., Ribosomal protein L5 facilitates rDNA-bundled condensate and
721 nucleolar assembly. *Life Sci. Alliance* **5,** e202101045 (2022).

722 33. S Banani, H Lee, A Hyman, M Rosen, Biomolecular condensates: organizers of
723 cellular biochemistry. *Nat. Rev. Mol. Cell Biol.* **18,** 285–298 (2017).

724 34. Y Shin, C Brangwynne, Liquid phase condensation in cell physiology and disease.
725 *Science* **357,** eaaf4382 (2017).

726 35. T Yamamoto, T Yamazaki, T Hirose, Phase separation driven by production of
727 architectural RNA transcripts. *Soft Matter* **16,** 4692–4698 (2020).

728 36. D Langevin, Microemulsion, *Acc. Chem. Res.* **21,** 255-260 (1988).

729 37. AW Folkmann, A Putnam, CF Lee, and G Seydoux, Regulation of biomolecular
730 condensates by interfacial protein clusters. Science. 373, 1218-1224 (2021).

731 38. MGJ Navarro, S Kashida, R Chouaib, S Souquere, G Pierron, D Weil, and Z Gueroui,
732 RNA is a critical element for the sizing and the composition of phase-separated RNA-
733 protein condensates. Nat. Comm., 10, 3230 (2019).

734 39. M Wu, et al., lncRNA SLERT controls phase separation of FC/DFCs to facilitate Pol
735 I transcription. *Science* **373,** 547–555 (2021).

736 40. T W Turowski and D Tollervery, Cotranscriptional events in eukaryotic ribosome
737 synthesis. *WIREs RNA* **6,** 129-139.

738 41. J Barandun, M Hunziker, and S Klinge, Assembly and structure of the SSU
739 processome – a nucleolar precursor of the small ribosomal submit. *Curr. Opin. Struct.*
740 *Biol.* **49,** 85-93.

741 42. R. Tomecki, P J Sikorski, M Zakrzewska-Placzek. Comparison of preribosomal RNA
742 processing pathways in yeast, plant, and human cells – focus on coordinated action of
743 endo- and exoribonulease. *FEBS Lett.* **591,** 1801-1850.

744 43. C E Scull and D A Schneider. Coordinated control of rRNA processing by RNA
745 polymerase I. *Trends Genet.* **35,** 724-733.

746 44. A Tartakoff, P DiMario, E Hurt, B McStay, V G Panse, and D Tollervery, The dual
747 nature of the nucleolus. *Genes Dev.* **36,** 765-769 (2022).

748 45. J Henninger, et al., RNA-Mediated Feedback Control of Transcriptional Condensates.
749 *Cell* **184,** 207–225 (2021).

750 46. L Hilbert, et al., Transcription organizes euchromatin via microphase separation. *Nat.*
751 *Comms.* **12,** 1360 (2021).

752 47. T Nozaki, et al., Dynamic Organization of Chromatin Domains Revealed by Super-
753 Resolution Live-Cell Imaging. *Mol. Cell* **67,** 282–293 (2017).

754 48. B Sabari, et al., Coactivator condensation at super-enhancers links phase separation
755 and gene control. *Science* **361,** eaar3958 (2018).

756 49. M Wei, et al., Nucleated transcriptional condensates amplify gene expression. *Nat.*
757 *Cell Biol.* **22,** 1187–1196 (2020).

758 50. T Kawaguchi, et al., SWI/SNF chromatin-remodeling complexes function in
759 noncoding RNA-dependent assembly of nuclear bodies. *Proc. Natl. Acad. Sci. USA* **112,**
760 4304–4309 (2015).

761 51. G Biamonti, C Vourc'h, Nuclear Stress Bodies. *Cold Spring Harb. Perspect. Biol.* **2,**
762 a000695 (2010).

763 52. K Ninomiya, et al., LncRNA-dependent nuclear stress bodies promote intron
764 retention through SR protein phosphorylation. *EMBO J.* **39,** e102729 (2020).

765 53. K Ninomiya, T Hirose, Short Tandem Repeat-Enriched Architectural RNAs in Nuclear
766 Bodies: Functions and Associated Disease. *non-coding RNA* **6,** 6 (2020).

767 54. P de Gennes, Conformation of polymers attached to an interface. *Macromolecules*
768 **13,** 1069–1075 (1980).

769 55. M Daoud, J Cotton, Star shaped polymers: a model for the conformation and its
770 concentration dependence. *J. Phys. France* **43,** 531–538 (1982).

771

FIGURE LEGENDS

Figure 1 Multiphase structure of a nucleolus. (A) A nucleolus is composed of multiple fibrillar center (FC) microphases in the sea of the granular component (GC). There is a layer of dense fibrillar component (DFC) between each FC and GC. (B) RNA polymerase I (Pol I) molecules (white particles) are entrapped in FC microphases (light blue) and the active rDNA units (black line) are localized at the surfaces of microphases. Nascent pre-rRNAs (green particles) are thus at the surfaces of the microphase and form a DFC layer with RNA-binding proteins (magenta particles). The interface between FC and DFC is located at a distance r_{in} from the center and the interface between DFC and GC is located at a distance r_{ex}.

Figure 2 Model of transcription dynamics. DNA (black solid line) is localized at the surface of an FC (cyan). (A) RNA polymerase I (Pol I) in a microphase binds to the transcription starting site (TSS) of an active rDNA repeat unit. The bound Pol I starts transcription with the rate k_{e} or returns to the microphase without starting transcription. (B) During the transcription, Pol I migrates uni-directionally towards the transcription terminating site (TTS) while polymerizing a nascent pre-rRNA. The terminal region of the nascent pre-ribosomal RNA (pre-rRNA), to which fibrillarin binds, are cleaved by the co-transcriptional RNA processing with the rate τ_{pr}^{-1}. The terminal region is released to GC. (C) After the cleavage of the terminal region, Pol I continues transcription until it reaches the TTS. At the TTS, Pol I is releaed to the FC with the rate τ_0^{-1}.

Figure 3 Composition of planer DFC layer vs interaction parameter χ. (A) The volume fraction ϕ_{r} of pre-rRNA units (green), the volume fraction ϕ_{p} of freely diffusing RBPs (magenta), the volume fraction ϕ_{s} of solvent molecules (cyan) in a DFC layer are shown as functions of the interaction parameter χ. (B) The occupancy α_{p} of pre-rRNA terminal region by RBPs is shown as a function of the interaction parameter χ. We used $\mu_p/(k_{\mathrm{B}}T) = -10.0$, $\epsilon = -12.0$, $\sigma_{\mathrm{in}}b^2 = 0.05$, and $\Pi_{\mathrm{ex}}b^3/(k_{\mathrm{B}}T) = 0.0$ for the calculations, see also Table 2. The solid lines are derived by numerically solving eqs. S15, S16, and S20 in the SI Appendix. The broken lines are derived by using eqs. S47 (shown for $\chi > 10.1$).

Figure 4 Profile of volume fraction ϕ_{r} of pre-rRNA units in DFC layer. The volume fraction of nascent pre-rRNA units is shown as a function of the position r in the DFC layer ($r_{\mathrm{in}} < r < r_{\mathrm{ex}}$). The solid dark green line is derived by numerically calculating eqs. S13, S15, and S16 in the SI Appendix for $\zeta = 0.06$ with the condition that the volume fraction of solvent is zero and the occupancy of the terminal regions of pre-rRNAs by

RBPs is unity. The values of other parameters are summarized in Table 2. The broken light green line is derived by using eq. S59 in the SI Appendix with $\phi_{\mathrm{ex}} = 0.0157$ and $r_{\mathrm{ex}} = 1.98$ (which were derived from the numerical calculation to obtain the light green line). The volume fraction of freely diffusing RBPs is shown in the inset.

Figure 5 Free energy F of nucleolus. The free energy F of the system is shown as a function of the radius r_{in} of FCs (A) and the ratio $r_{\mathrm{ex}}/r_{\mathrm{in}}$ of the external radius to the internal radius (B). The black solid line is the total free energy, including the free energy of DFC layers (shown by the magenta broken line, the first term of eq. 2) and the surface free energy (shown by the cyan broken line, the second and third terms of eq. 2) for $\zeta = 0.06$. The values of other parameters are summarized in Table 2.

Figure 6 Radius r_{in} of FCs vs rescaled transcription rate ζ. The radius r_{in} of FCs at the free energy minimum is shown as a function of rescaled transcription rate ζ. The solid dark green line is derived by numerically calculating eqs. S13, S15, and S16 in the SI Appendix with the condition that the volume fraction of solvent is zero and the occupancy of the terminal regions of pre-rRNAs by RBPs is unity. The orange broken line is derived by using eq. 5. The parameters used for the calculations are summarized in Table 2.

Figure 7 Mild Pol I inhibition by BMH-21 increases the size of FCs. (A) Immunofluorescence of UBF (FC) and NPM1 (GC) in HeLa cells with or without BMH-21 treatments. Scale bar, 10 μm. (B and C) Quantification of longest axis (B) and area (C) of the FCs in cells under indicated conditions. Each scatter dot plot shows the mean (black line). Dots indicate all points of quantified data (n = 250). Mean longest axes of the FCs is shown below: 0 μM: 0.4907 μm, 0.0625 μM: 0.7440 μm, 0.125 μM: 0.8710 μm, 0.25 μM: 1.131 μm. Mean areas of the FCs are shown below: 0 μM: 0.170 μm^2, 0.0625 μM: 0.3255 μm^2, 0.125 μM: 0.4347 μm^2, 0.25 μM: 0.7312 μm^2. Statistical analyses using Kruskal-Wallis test with Dunn's multiple comparison test were performed and the results are shown as follows. (B) 0 μM vs 0.0625 μM: P < 0.0001, 0 μM vs 0.125 μM: P < 0.0001, 0 μM vs 0.25 μM: P < 0.0001, 0.0625 μM vs 0.125 μM: P < 0.0001, 0.0625 μM vs 0.25 μM: P < 0.0001, 0.125 μM vs 0.25 μM: P = 0.0008. (C) 0 μM vs 0.0625 μM: P = 0.0003, 0 μM vs 0.125 μM: P < 0.0001, 0 μM vs 0.25 μM: P < 0.0001, 0.0625 μM vs 0.125 μM: P < 0.0001, 0.0625 μM vs 0.25 μM: P < 0.0001, 0.125 μM vs 0.25 μM: P = 0.0010. (D and E) Graphs showing the mean longest axis (D) and area (E) of the FCs with SEM vs pre-rRNA expression levels. The pre-rRNA expression level in untreated cells is defined as 1.

840 **Figure 8 Exponent that accounts for the dependence of the size of FCs on pre-**
841 **rRNA expression level.** The data in Fig. 7E was shown in the double-logarithm plot and
842 fitted with a power function. The magenta and cyan dots are the results by suppressing
843 the Pol I transcription by using BMH-21 and CX-5461. The slope of the double-logarithm
844 plot is the exponent that accounts for the dependence of the radius of FCs on the
845 transcription level. The curve fitting shows that the exponent is -0.49 for the case of the
846 BMH-21 treatment, -0.46 for the case of the CX-5461, and -0.48 if both data are fitted.

847 **Figure 9 Summary of results.** RNP complexes enhance or suppress the growth of
848 condensates depending on whether the RNP complexes are mobile in the interior or
849 tethered to the surfaces of the condensates. A. The multivalent interaction between the
850 RNP complexes enhance the growth of the condensates if these condensates are
851 assembled by the RNP complexes. B. The multivalent interaction between the RNP
852 complexes suppress the growth of the condensates if these complexes are tethered to
853 the surfaces of the condensates assembled by other RNAs and proteins.
854
855

LEGENDS OF SUPPLEMENTARY FIGURES

Figure S1 BMH-21 and CX-5461 treatment reduce pre-rRNA expression levels in a dose-dependent manner.
(*A*) Quantification of pre-rRNA expression levels by RT-qPCR in BMH-21-untreated and -treated conditions. Data are represented as mean ± SD (*n* =3). (*B*) Quantification of pre-rRNA expression levels by RT-qPCR in CX-5461-untreated and -treated conditions. Data are represented as mean ± SD (*n* =3).

Figure S2 FCs and DFCs in the BMH-21 and CX-5461-untreated and -treated cells.
(*A* and *B*) Immunofluorescence of UBF (FC) and FBL (DFC) in HeLa cells with or without BMH-21 (*A*) or CX-5461 (*B*) treatments. Scale bar, 10 μm.

Figure S3 Mild Pol I inhibition by CX-5461 increases the size of FCs.
(*A*) Immunofluorescence of UBF (FC) and NPM1 (GC) in HeLa cells with or without CX-5461 treatments. In the cells treated with 2 μM CX-5461, the cells with large granules (upper) or nucleolar caps (lower) were observed. Scale bar, 10 μm. (*B* and *C*) Quantification of longest axis (*B*) and area (*C*) of the FCs in cells under indicated conditions. Each scatter dot plot shows the mean (black line). Dots indicate all points of quantified data (*n* = 500). Mean longest axes of the FCs is shown below: 0 μM: 0.5196 μm, 0.25 μM: 0.6367 μm, 0.5 μM: 0.7192 μm, 1 μM: 1.059 μm. Mean areas of the FCs are shown below: 0 μM: 0.1155 μm^2, 0. 25 μM: 0.2171 μm^2, 0.5 μM: 0.3058 μm^2, 1 μM: 0.6544 μm^2. Statistical analyses using Kruskal-Wallis test with Dunn's multiple comparison test were performed and the results are shown as follows. (*B*) 0 μM vs 0.25 μM: $P < 0.0001$, 0 μM vs 0.5 μM: $P < 0.0001$, 0 μM vs 1 μM: $P < 0.0001$, 0.25 μM vs 0.5 μM: $P = 0.0211$, 0.25 μM vs 1 μM: $P < 0.0001$, 0.5 μM vs 1 μM: $P < 0.0001$. (*C*) 0 μM vs 0.25 μM: $P < 0.0001$, 0 μM vs 0.5 μM: $P < 0.0001$, 0 μM vs 1 μM: $P < 0.0001$, 0.25 μM vs 0.5 μM: $P = 0.0012$, 0.25 μM vs 1 μM: $P < 0.0001$, 0.5 μM vs 1 μM: $P < 0.0001$. (*D* and *E*) Graphs showing the mean longest axis (*D*) and area (*E*) of the FCs with SEM vs pre-rRNA expression levels. The pre-rRNA expression level in untreated cells is defined as 1.

Figure S4 Quantification of the FCs in the nucleoli
Screenshots of detections of FCs and GCs by NIS Elements Advanced Research software (NIKON) are shown. Green circles indicate UBF foci, and red circles indicate nucleoli labeled by NPM1 antibodies. UBF foci detected in the nucleoli (lower right) were quantified.

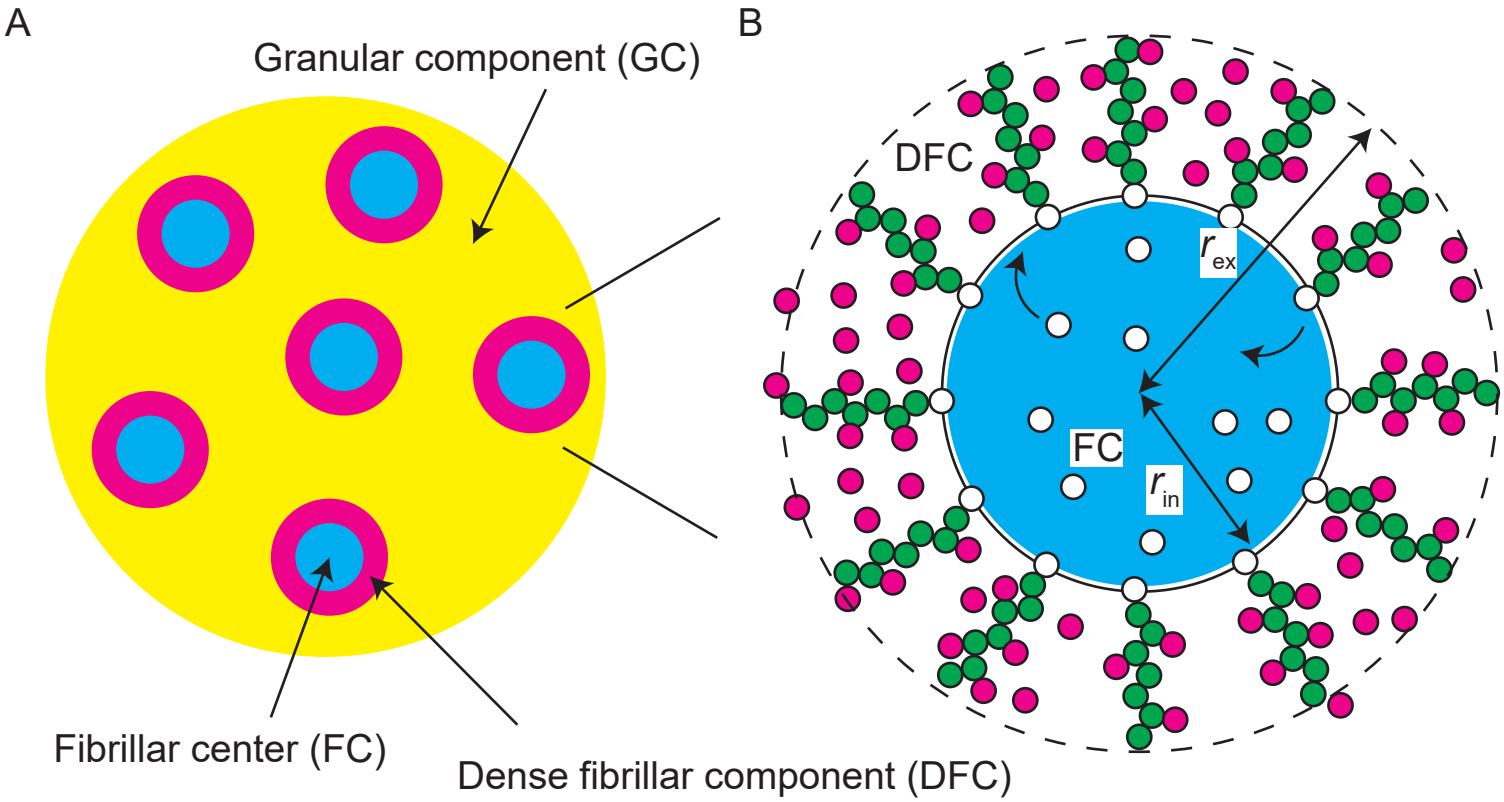

Figure 1 Multi-phase structure of a nucleolus. (A) A nucleolus is composed of multiple fibrillar center (FC) microphases in the sea of the granular component (GC). There is a layer of dense fibrillar component (DFC) between each FC and GC. (B) RNA polymerase I (Pol I) molecules (white particles) are entrapped in FC microphases (light blue) and the active rDNA units (black line) are localized at the surfaces of microphases. Nascent pre-rRNA transcripts (green particles) are thus at the surfaces of the microphase and form a DFC layer with RNA-binding proteins (magenta particles). The interface between FC and DFC is located at a distance r_{in} from the center and the interface between DFC and GC is located at a distance r_{ex}.

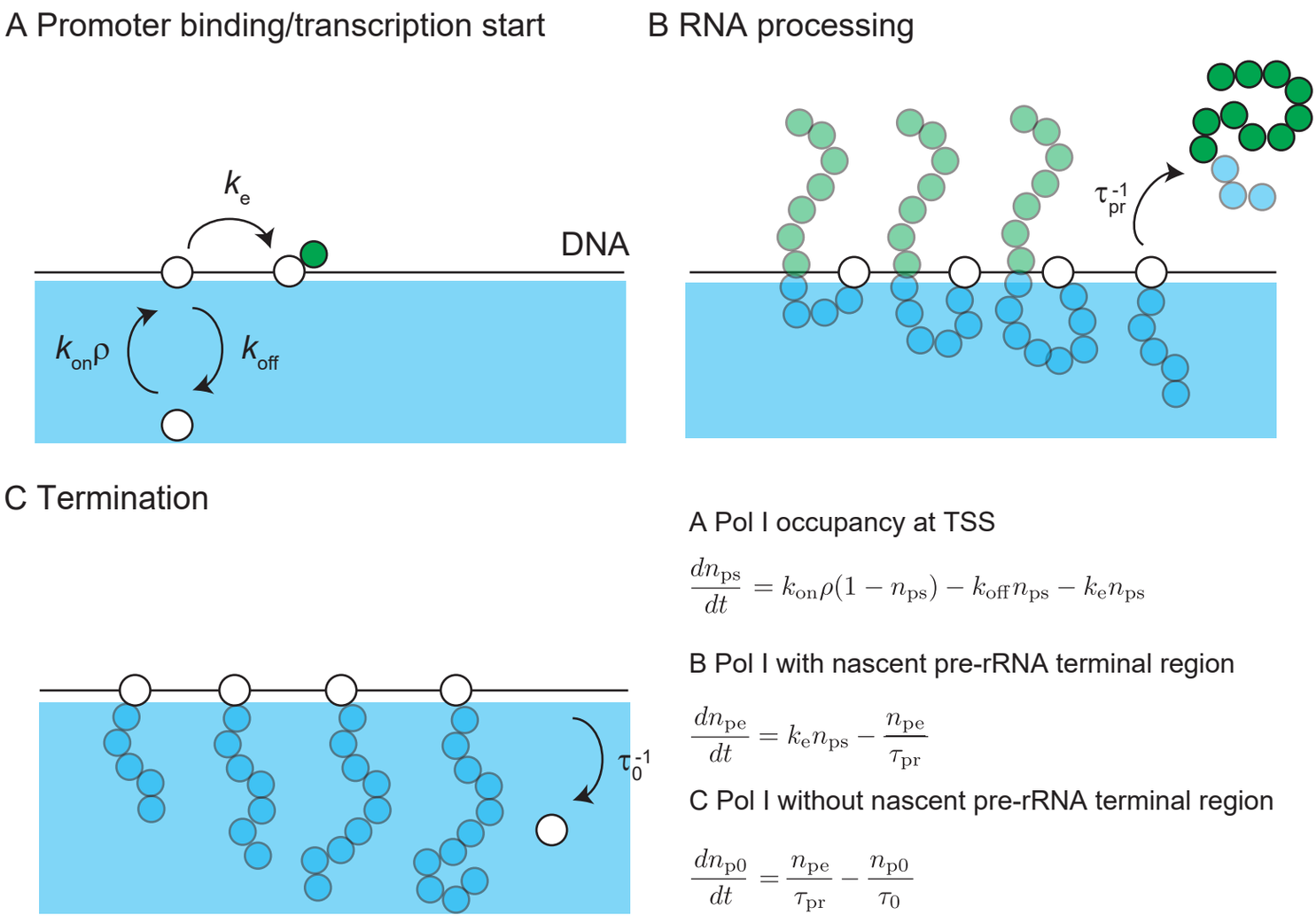

Figure 2 Model of transcription dynamics. DNA (black solid line) is localized at the surface of an FC (cyan). (A) RNA polymerase I (Pol I) in a microphase binds to the transcription starting site (TSS) of an active rDNA repeat unit. The bound Pol I starts transcription with the rate k_e or returns to the microphase without starting transcription. (B) During the transcription, Pol I migrates uni-directionally towards the transcription terminating site (TTS) while polymerizing a nascent pre-rRNA. The terminal region of the nascent pre-ribosomal RNA (pre-rRNA), to which fibrillarin binds, are cleaved by the co-transcriptional RNA processing with the rate τ_{pr}^{-1}. The terminal region is released to GC. (C) After the cleavage of the terminal region, Pol I continues transcription until it reaches the TTS. At the TTS, Pol I is releaed to the FC with the rate τ_0^{-1}.

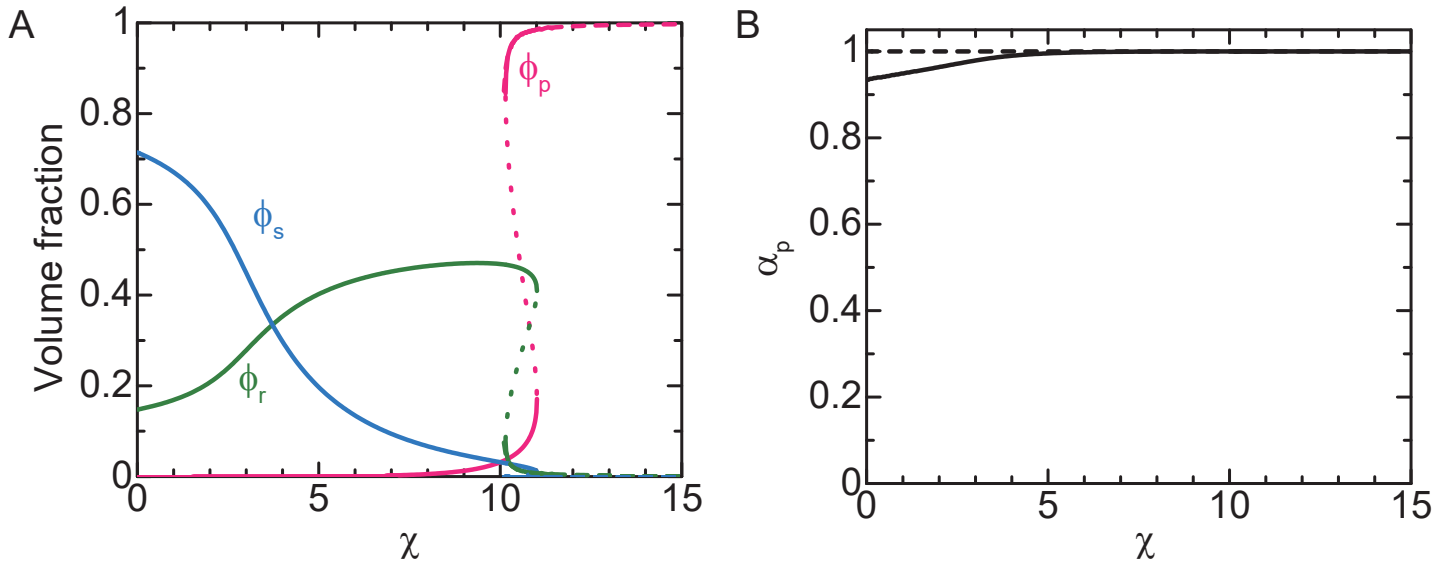

Figure 3 Composition of planer DFC layer vs interaction parameter χ. (A) The volume fraction φ_r of pre-rRNA units (green), the volume fraction φ_p of freely diffusing RBPs (magenta), the volume fraction φ_s of solvent molecules (cyan) in a DFC layer are shown as functions of the interaction parameter χ. (B) The occupancy α_p of RNA terminal region by RBPs is shown as a function of the interaction parameter χ. We used $\mu_p/(k_BT)$=-10.0, ε=-12.0, $\sigma_{in}b^2$=0.05, and $\Pi_{ex}b^3/(k_BT)$=0.0 for the calculations, see also Table 1. The solid lines are derived by numerically solving eqs. S15, S16, and S20 in the SI Appendix. The broken lines are derived by using eqs. S47 (shown for χ>10.1).

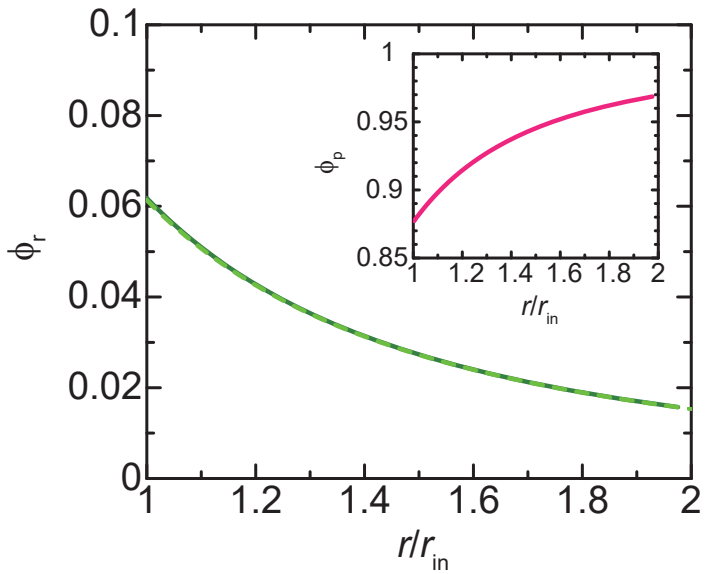

Figure 4 Profile of volume fraction φ_r of pre-rRNA units in DFC layer. The volume fraction of nascent pre-rRNA units is shown as a function of the position r in the DFC layer ($r_{in}<r<r_{ex}$). The solid dark green line is derived by numerically calculating eqs. S13, S15, and S16 in the SI Appendix for ζ=0.06 with the condition that the volume fraction of solvent is zero and the occupancy of the terminal regions of pre-rRNAs by RBPs is unity. The values of other parameters are summarized in Table 1. The broken light green line is derived by using eq. S59 in the SI Appendix with φ_{ex}=0.0157 and r_{ex}=1.98 (which were derived from the numerical calculation to obtain the light green line). The volume fraction of freely diffusing RBPs is shown in the inset.

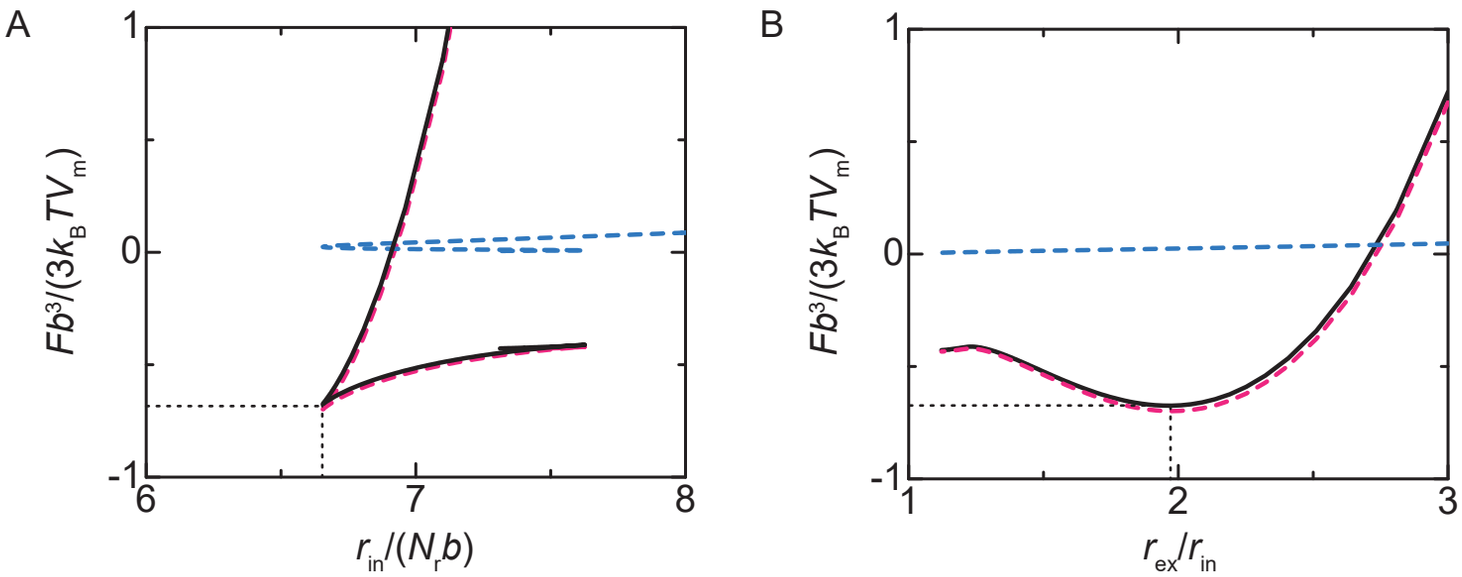

Figure 5 Free energy *F* of nucleolus. The free energy *F* of the system is shown as a function of the radius r_{in} of FCs (a) and the ratio r_{ex}/r_{in} of the external radius to the internal radius (b). The black solid line is the total free energy, including the free energy of DFC layers (shown by the magenta broken line, the first term of eq. 2) and the surface free energy (shown by the cyan broken line, the second and third terms of eq. 2) for ζ=0.06. The values of other parameters are summarized in Table 1.

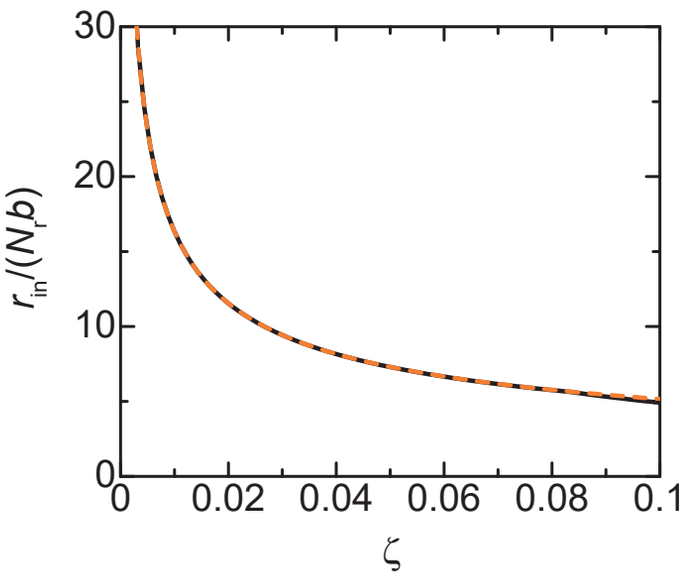

Figure 6 Radius r_{in} of FCs vs rescaled transcription rate ζ. The radius r_{in} of FCs at the free energy minimum is shown as a function of rescaled transcription rate ζ. The solid dark green line is derived by numerically calculating eqs. S13, S15, and S16 in the SI Appendix with the condition that the volume fraction of solvent is zero and the occupancy of the terminal regions of pre-rRNAs by RBPs is unity. The orange broken line is derived by using eq. 5. The parameters used for the calculations are summarized in Table 1.

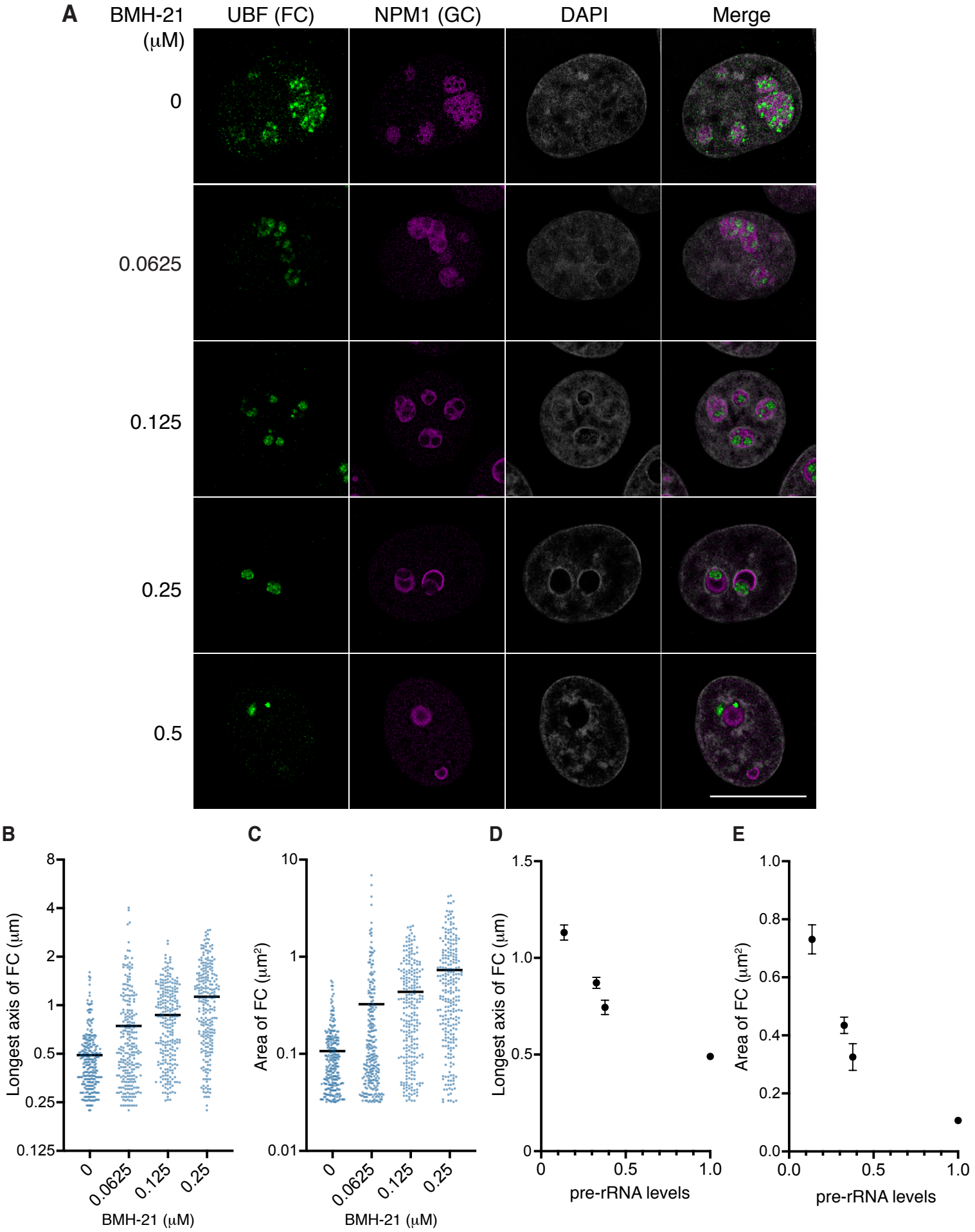
A
BMH-21 (μM)
UBF (FC)
NPM1 (GC)
DAPI
Merge
0
0.0625
0.125
0.25
0.5
B
Longest axis of FC (μm)
8
4
2
1
0.5
0.25
0.125
0
0.0625
0.125
0.25
BMH-21 (μM)
C
Area of FC (μm²)
10
1
0.1
0.01
0
0.0625
0.125
0.25
BMH-21 (μM)
D
Longest axis of FC (μm)
1.5
1.0
0.5
0
0
0.5
1.0
pre-rRNA levels
E
Area of FC (μm²)
1.0
0.8
0.6
0.4
0.2
0.0
0.0
0.5
1.0
pre-rRNA levels

Figure 7 Mild Pol I inhibition by BMH-21 increases the size of FCs. (A) Immunofluorescence of UBF (FC) and NPM1 (GC) in HeLa cells with or without BMH-21 treatments. Scale bar, 10 μm. (B and C) Quantification of longest axis (B) and area (C) of the FCs in cells under indicated conditions. Each scatter dot plot shows the mean (black line). Dots indicate all points of quantified data (n = 250). Mean longest axes of the FCs is shown below: 0 μM: 0.4907 μm, 0.0625 μM: 0.7440 μm, 0.125 μM: 0.8710 μm, 0.25 μM: 1.131 μm. Mean areas of the FCs are shown below: 0 μM: 0.170 μm^2, 0.0625 μM: 0.3255 μm^2, 0.125 μM: 0.4347 μm^2, 0.25 μM: 0.7312 μm^2. Statistical analyses using Kruskal-Wallis test with Dunn's multiple comparison test were performed and the results are shown as follows. (B) 0 μM vs 0.0625 μM: $P < 0.0001$, 0 μM vs 0.125 μM: $P < 0.0001$, 0 μM vs 0.25 μM: $P < 0.0001$, 0.0625 μM vs 0.125 μM: $P < 0.0001$, 0.0625 μM vs 0.25 μM: $P < 0.0001$, 0.125 μM vs 0.25 μM: $P = 0.0008$. (C) 0 μM vs 0.0625 μM: $P = 0.0003$, 0 μM vs 0.125 μM: $P < 0.0001$, 0 μM vs 0.25 μM: $P < 0.0001$, 0.0625 μM vs 0.125 μM: $P < 0.0001$, 0.0625 μM vs 0.25 μM: $P < 0.0001$, 0.125 μM vs 0.25 μM: $P = 0.0010$. (D and E) Graphs showing the mean longest axis (D) and area (E) of the FCs with SEM vs pre-rRNA expression levels. The pre-rRNA expression level in untreated cells is defined as 1.

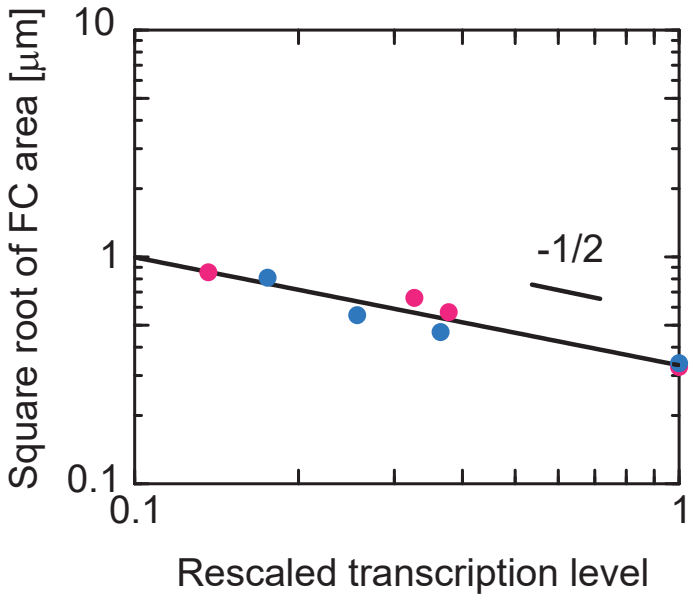

Figure 8 Exponent that account for the dependence of the size of FCs on pre-rRNA expression level. The data in Fig. 7E was shown in the double-logarithm plot and fitted with a power function. The magenta and cyan dots are the results by suppressing the Pol I transcription by using BMH-21 and CX-5461. The slope of the double-logarithm plot is the exponent that accounts for the dependence of the radius of FCs on the transcription level. The curve fitting shows that the exponent is -0.49 for the case of the BMH-21 treatment, -0.46 for the case of the CX-5461 treatment, and -0.48 if both data are used.

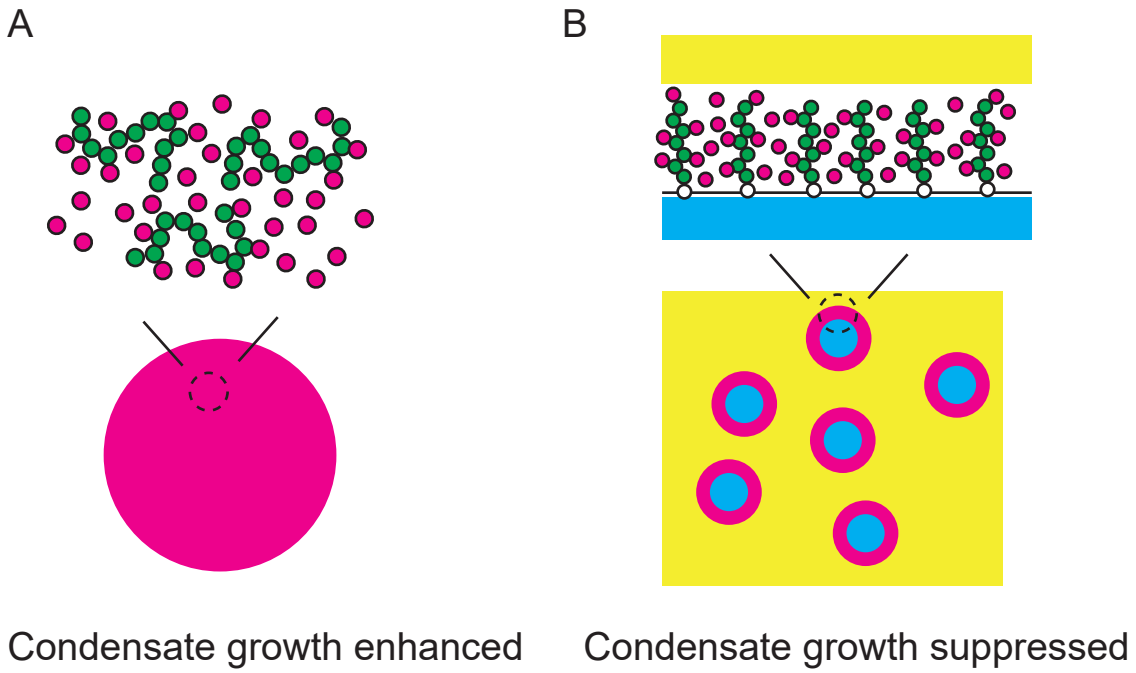

Figure 9 Summary of results. RNP complexes of RNAs and RBPs enhance or suppress the growth of condensates depending on whether the RNP complexes are mobile in the interior or tethered to the surfaces of the condensates. A. The multi-valent interaction between the RNP complexes enhance the growth of the condensates if these condensates are assembled by the RNP complexes. B. The multi-valent interaction between the RNP complexes suppress the growth of the condensates if these complexes are tethered to the surfaces of the condensates assembled by other RNAs and proteins.